Title

Hadronic resonance production in d+Au collisions at sNN=200 GeV measured at the BNL Relativistic Heavy Ion Collider

Journal

Physical Review C, 78(4)

ISSN

2469-9985

Authors

Abelev, BI
Aggarwal, MM
Ahammed, Z
et al.

Publication Date

2008-10-01

DOI

10.1103/physrevc.78.044906

Peer reviewed

Hadronic resonance production in d+Au collisions at $\sqrt{s_{NN}} = 200$ GeV measured at the BNL Relativistic Heavy Ion Collider

B. I. Abelev,[9] M. M. Aggarwal,[30] Z. Ahammed,[46] B. D. Anderson,[19] D. Arkhipkin,[13] G. S. Averichev,[12] Y. Bai,[28] J. Balewski,[23] O. Barannikova,[9] L. S. Barnby,[2] J. Baudot,[17] S. Baumgart,[51] D. R. Beavis,[3] R. Bellwied,[49] F. Benedosso,[28] R. R. Betts,[9] S. Bhardwaj,[35] A. Bhasin,[18] A. K. Bhati,[30] H. Bichsel,[48] J. Bielcik,[11] J. Bielcikova,[11] B. Biritz,[6] L. C. Bland,[3] M. Bombara,[2] B. E. Bonner,[36] M. Botje,[28] J. Bouchet,[19] E. Braidot,[28] A. V. Brandin,[26] Bruna,[51] S. Bueltmann,[3] T. P. Burton,[2] M. Bystersky,[11] X. Z. Cai,[39] H. Caines,[51] M. Calderón de la Barca Sánchez,[5] J. Callner,[9] O. Catu,[51] D. Cebra,[5] R. Cendejas,[6] M. C. Cervantes,[41] Z. Chajecki,[29] P. Chaloupka,[11] S. Chattopdhyay,[46] H. F. Chen,[38] J. H. Chen,[39] J. Y. Chen,[50] J. Cheng,[43] M. Cherney,[10] A. Chikanian,[51] K. E. Choi,[34] W. Christie,[3] S. U. Chung,[3] R. F. Clarke,[41] M. J. M. Codrington,[41] J. P. Coffin,[17] T. M. Cormier,[49] M. R. Cosentino,[37] J. G. Cramer,[48] H. J. Crawford,[4] D. Das,[5] S. Dash,[14] M. Daugherity,[42] C. De Silva,[49] T. G. Dedovich,[12] M. DePhillips,[3] A. A. Derevschikov,[32] R. Derradi de Souza,[7] L. Didenko,[3] P. Djawotho,[16] S. M. Dogra,[18] X. Dong,[22] J. L. Drachenberg,[41] J. E. Draper,[5] F. Du,[51] J. C. Dunlop,[3] M. R. Dutta Mazumdar,[46] W. R. Edwards,[22] L. G. Efimov,[12] E. Elhalhuli,[2] M. Elnimr,[49] V. Emelianov,[26] J. Engelage,[4] G. Eppley,[36] B. Erazmus,[40] M. Estienne,[17] L. Eun,[31] P. Fachini,[3] R. Fatemi,[20] J. Fedorisin,[12] A. Feng,[50] P. Filip,[13] E. Finch,[51] V. Fine,[3] Y. Fisyak,[3] C. A. Gagliardi,[41] L. Gaillard,[2] D. R. Gangaharan,[6] M. S. Ganti,[46] E. Garcia-Solis,[9] V. Ghazikhanian,[6] P. Ghosh,[46] Y. N. Gorbunov,[10] A. Gordon,[3] O. Grebenyuk,[22] D. Grosnick,[45] B. Grube,[34] S. M. Guertin,[6] K. S. F. F. Guimaraes,[37] A. Gupta,[18] N. Gupta,[18] W. Guryn,[3] B. Haag,[5] T. J. Hallman,[3] A. Hamed,[41] J. W. Harris,[51] W. He,[16] M. Heinz,[51] S. Hepplemann,[31] B. Hippolyte,[17] A. Hirsch,[33] A. M. Hoffman,[23] G. W. Hoffmann,[42] D. J. Hofman,[9] R. S. Hollis,[9] H. Z. Huang,[6] T. J. Humanic,[29] G. Igo,[6] A. Iordanova,[9] P. Jacobs,[22] W. W. Jacobs,[16] P. Jakl,[11] F. Jin,[39] P. G. Jones,[2] J. Joseph,[19] E. G. Judd,[4] S. Kabana,[40] K. Kajimoto,[42] K. Kang,[43] J. Kapitan,[11] M. Kaplan,[8] D. Keane,[19] A. Kechechyan,[12] D. Kettler,[48] V. Yu. Khodyrev,[32] J. Kiryluk,[22] A. Kisiel,[29] S. R. Klein,[22] A. G. Knospe,[51] A. Kocoloski,[23] D. D. Koetke,[45] M. Kopytine,[19] L. Kotchenda,[26] V. Kouchpil,[11] P. Kravtsov,[26] V. I. Kravtsov,[32] K. Krueger,[1] M. Krus,[11] C. Kuhn,[17] L. Kumar,[30] P. Kurnadi,[6] M. A. C. Lamont,[3] J. M. Landgraf,[3] S. LaPointe,[49] J. Lauret,[3] A. Lebedev,[3] R. Lednicky,[13] C.-H. Lee,[34] M. J. LeVine,[3] C. Li,[38] Y. Li,[43] G. Lin,[51] X. Lin,[50] S. J. Lindenbaum,[27] M. A. Lisa,[29] F. Liu,[50] H. Liu,[5] J. Liu,[36] L. Liu,[50] T. Ljubicic,[3] W. J. Llope,[36] R. S. Longacre,[3] W. A. Love,[3] Y. Lu,[38] T. Ludlam,[3] D. Lynn,[3] G. L. Ma,[39] Y. G. Ma,[39] D. P. Mahapatra,[14] R. Majka,[51] M. I. Mall,[5] L. K. Mangotra,[18] R. Manweiler,[45] S. Margetis,[19] C. Markert,[42] H. S. Matis,[22] Yu. A. Matulenko,[32] T. S. McShane,[10] A. Meschanin,[32] J. Millane,[23] M. L. Miller,[23] N. G. Minaev,[32] S. Mioduszewski,[41] A. Mischke,[28] D. K. Mishra,[14] J. Mitchell,[36] B. Mohanty,[46] D. A. Morozov,[32] M. G. Munhoz,[37] B. K. Nandi,[15] C. Nattrass,[51] T. K. Nayak,[46] J. M. Nelson,[2] C. Nepali,[19] P. K. Netrakanti,[33] M. J. Ng,[4] L. V. Nogach,[32] S. B. Nurushev,[32] G. Odyniec,[22] A. Ogawa,[3] H. Okada,[3] V. Okorokov,[26] D. Olson,[22] M. Pachr,[11] B. S. Page,[16] S. K. Pal,[46] Y. Pandit,[19] Y. Panebratsev,[12] T. Pawlak,[47] T. Peitzmann,[28] V. Perevoztchikov,[3] C. Perkins,[4] W. Peryt,[47] S. C. Phatak,[14] M. Planinic,[52] J. Pluta,[47] N. Poljak,[52] A. M. Poskanzer,[22] B. V. K. S. Potukuchi,[18] D. Prindle,[48] C. Pruneau,[49] N. K. Pruthi,[30] J. Putschke,[51] R. Raniwala,[35] S. Raniwala,[35] R. L. Ray,[42] R. Reed,[5] A. Ridiger,[26] H. G. Ritter,[22] J. B. Roberts,[36] O. V. Rogachevskiy,[12] J. L. Romero,[5] A. Rose,[22] C. Roy,[40] L. Ruan,[3] M. J. Russcher,[28] V. Rykov,[19] R. Sahoo,[40] I. Sakrejda,[22] T. Sakuma,[23] S. Salur,[22] J. Sandweiss,[51] M. Sarsour,[41] J. Schambach,[42] R. P. Scharenberg,[33] N. Schmitz,[24] J. Seger,[10] I. Selyuzhenkov,[16] P. Seyboth,[24] A. Shabetai,[17] E. Shahaliev,[12] M. Shao,[38] M. Sharma,[49] S. S. Shi,[50] X-H. Shi,[39] E. P. Sichtermann,[22] F. Simon,[24] R. N. Singaraju,[46] M. J. Skoby,[33] N. Smirnov,[51] R. Snellings,[28] P. Sorensen,[3] J. Sowinski,[16] H. M. Spinka,[1] B. Srivastava,[33] A. Stadnik,[12] T. D. S. Stanislaus,[45] D. Staszak,[6] M. Strikhanov,[26] B. Stringfellow,[33] A. A. P. Suaide,[37] M. C. Suarez,[9] N. L. Subba,[19] M. Sumbera,[11] X. M. Sun,[22] Y. Sun,[38] Z. Sun,[21] B. Surrow,[23] T. J. M. Symons,[22] A. Szanto deToledo,[37] J. Takahashi,[7] A. H. Tang,[3] Z. Tang,[38] T. Tarnowsky,[33] D. Thein,[42] J. H. Thomas,[22] J. Tian,[39] A. R. Timmins,[2] S. Timoshenko,[26] Tlusty,[11] M. Tokarev,[12] T. A. Trainor,[48] V. N. Tram,[22] A. L. Trattner,[4] S. Trentalange,[6] R. E. Tribble,[41] O. D. Tsai,[6] J. Ulery,[33] T. Ullrich,[3] D. G. Underwood,[1] G. Van Buren,[3] M. van Leeuwen,[28] A. M. Vander Molen,[25] J. A. Vanfossen Jr.,[19] R. Varma,[15] G. M. S. Vasconcelos,[7] I. M. Vasilevski,[13] A. N. Vasiliev,[32] F. Videbaek,[3] S. E. Vigdor,[16] Y. P. Viyogi,[14] S. Vokal,[12] S. A. Voloshin,[49] M. Wada,[42] W. T. Waggoner,[10] F. Wang,[33] G. Wang,[6] J. S. Wang,[21] Q. Wang,[33] X. Wang,[43] X. L. Wang,[38] Y. Wang,[43] J. C. Webb,[45] G. D. Westfall,[25] C. Whitten Jr.,[6] H. Wieman,[22] S. W. Wissink,[16] R. Witt,[44] Y. Wu,[50] N. Xu,[22] Q. H. Xu,[22] Y. Xu,[38] Z. Xu,[3] P. Yepes,[36] I.-K. Yoo,[34] Q. Yue,[43] M. Zawisza,[47] H. Zbroszczyk,[47] W. Zhan,[21] H. Zhang,[3] S. Zhang,[39] W. M. Zhang,[19] Y. Zhang,[38] Z. P. Zhang,[38] Y. Zhao,[38] C. Zhong,[39] J. Zhou,[36] R. Zoulkarneev,[13] Y. Zoulkarneeva,[13] and J. X. Zuo[39]

(STAR Collaboration)

[1]*Argonne National Laboratory, Argonne, Illinois 60439, USA*

[2]*University of Birmingham, Birmingham, United Kingdom*

[3]*Brookhaven National Laboratory, Upton, New York 11973, USA*

[4]*University of California, Berkeley, California 94720, USA*

[5]*University of California, Davis, California 95616, USA*

[6]*University of California, Los Angeles, California 90095, USA*

[7]*Universidade Estadual de Campinas, Sao Paulo, Brazil*

[8]*Carnegie Mellon University, Pittsburgh, Pennsylvania 15213, USA*

[9]*University of Illinois at Chicago, Chicago, Illinois 60607, USA*

[10]*Creighton University, Omaha, Nebraska 68178, USA*
[11]*Nuclear Physics Institute AS CR, 250 68 Řež/Prague, Czech Republic*
[12]*Laboratory for High Energy (JINR), Dubna, Russia*
[13]*Particle Physics Laboratory (JINR), Dubna, Russia*
[14]*Institute of Physics, Bhubaneswar 751005, India*
[15]*Indian Institute of Technology, Mumbai, India*
[16]*Indiana University, Bloomington, Indiana 47408, USA*
[17]*Institut de Recherches Subatomiques, Strasbourg, France*
[18]*University of Jammu, Jammu 180001, India*
[19]*Kent State University, Kent, Ohio 44242, USA*
[20]*University of Kentucky, Lexington, Kentucky 40506-0055, USA*
[21]*Institute of Modern Physics, Lanzhou, People's Republic of China*
[22]*Lawrence Berkeley National Laboratory, Berkeley, California 94720, USA*
[23]*Massachusetts Institute of Technology, Cambridge, MA 02139-4307, USA*
[24]*Max-Planck-Institut für Physik, Munich, Germany*
[25]*Michigan State University, East Lansing, Michigan 48824, USA*
[26]*Moscow Engineering Physics Institute, Moscow, Russia*
[27]*City College of New York, New York City, New York 10031, USA*
[28]*NIKHEF and Utrecht University, Amsterdam, The Netherlands*
[29]*Ohio State University, Columbus, Ohio 43210, USA*
[30]*Panjab University, Chandigarh 160014, India*
[31]*Pennsylvania State University, University Park, Pennsylvania 16802, USA*
[32]*Institute of High Energy Physics, Protvino, Russia*
[33]*Purdue University, West Lafayette, Indiana 47907, USA*
[34]*Pusan National University, Pusan, Republic of Korea*
[35]*University of Rajasthan, Jaipur 302004, India*
[36]*Rice University, Houston, Texas 77251, USA*
[37]*Universidade de Sao Paulo, Sao Paulo, Brazil*
[38]*University of Science & Technology of China, Hefei 230026, People's Republic of China*
[39]*Shanghai Institute of Applied Physics, Shanghai 201800, People's Republic of China*
[40]*SUBATECH, Nantes, France*
[41]*Texas A&M University, College Station, Texas 77843, USA*
[42]*University of Texas, Austin, Texas 78712, USA*
[43]*Tsinghua University, Beijing 100084, People's Republic of China*
[44]*United States Naval Academy, Annapolis, MD 21402, USA*
[45]*Valparaiso University, Valparaiso, Indiana 46383, USA*
[46]*Variable Energy Cyclotron Centre, Kolkata 700064, India*
[47]*Warsaw University of Technology, Warsaw, Poland*
[48]*University of Washington, Seattle, Washington 98195, USA*
[49]*Wayne State University, Detroit, Michigan 48201, USA*
[50]*Institute of Particle Physics, CCNU (HZNU), Wuhan 430079, People's Republic of China*
[51]*Yale University, New Haven, Connecticut 06520, USA*
[52]*University of Zagreb, Zagreb, HR-10002, Croatia*

(Received 2 January 2008; published 24 October 2008)

We present the first measurements of the $\rho(770)^0$, $K^*(892)$, $\Delta(1232)^{++}$, $\Sigma(1385)$, and $\Lambda(1520)$ resonances in d+Au collisions at $\sqrt{s_{NN}} = 200$ GeV, reconstructed via their hadronic decay channels using the STAR detector (the solenoidal tracker at the BNL Relativistic Heavy Ion Collider). The masses and widths of these resonances are studied as a function of transverse momentum p_T. We observe that the resonance spectra follow a generalized scaling law with the transverse mass m_T. The $\langle p_T \rangle$ of resonances in minimum bias collisions are compared with the $\langle p_T \rangle$ of π, K, and $\bar{p}$. The ρ^0/π^-, K^*/K^-, Δ^{++}/p, $\Sigma(1385)/\Lambda$, and $\Lambda(1520)/\Lambda$ ratios in d+Au collisions are compared with the measurements in minimum bias $p+p$ interactions, where we observe that both measurements are comparable. The nuclear modification factors ($R_{d\mathrm{Au}}$) of the ρ^0, K^*, and Σ^* scale with the number of binary collisions (N_{bin}) for $p_T > 1.2$ GeV/c.

DOI: 10.1103/PhysRevC.78.044906 PACS number(s): 25.75.Dw, 13.75.Cs

I. INTRODUCTION

Quantum chromodynamics (QCD) predicts that hadronic matter at high temperatures and/or high densities undergoes a phase transition to a system of deconfined partonic matter, the quark gluon plasma (QGP) [1]. Matter under such extreme conditions can be studied in the laboratory by colliding nuclei at very high energies. The Relativistic Heavy-Ion Collider (RHIC) at Brookhaven National Laboratory has provided a variety of collision systems at different beam energies, including collisions of Au+Au, d+Au, and p+p at $\sqrt{s_{NN}} =$ 200 GeV.

Resonances are strongly decaying particles with lifetimes $\times\, c$ that are of the order of the size of the hot and dense medium produced in heavy-ion collisions. As such, the measurement of resonances in Au+Au collisions compared with those of p+p collisions at $\sqrt{s_{NN}} =$ 200 GeV has provided detailed information about the interaction dynamics in relativistic heavy-ion collisions [2–7], where hadronic lifetimes and interaction cross sections affect the resonance yields [2,8–13].

The in-medium effects related to the high density and/or high temperature of the medium can modify the properties of short-lived resonances, such as their masses, widths, and even their spectral shapes [14–16]. Thus, resonances provide a unique tool for studying various properties of interaction dynamics in relativistic heavy-ion collisions [17,18]. A good understanding of resonance production in the reference systems p+p and d+Au is useful in understanding resonance production in Au+Au collisions. Comparisons between p+p and Au+Au for the ρ^0 and K^{*0} mesons have been made elsewhere [3,4], where it was observed that there were modifications of the resonance properties (mass and width) in both systems with respect to values in the vacuum in the absence of any medium effects. The measurement of masses and widths of resonances in d+Au collisions add further information to the existing measurements.

In addition, the regeneration of resonances and the rescattering of their daughters are two competing effects that affect the interpretation of resonance production. Resonances that decay before kinetic freeze-out (vanishing elastic collisions) may not be reconstructed due to the rescattering of the daughter particles. In this case, the resonance survival probability is relevant and depends on the time between chemical and kinetic freeze-outs, the source size, and the resonance transverse momentum p_T. On the other hand, after chemical freeze-out (vanishing inelastic collisions), elastic interactions may increase the resonance population compensating for the ones that decay before kinetic freeze-out. The case of resonance regeneration depends on the hadronic cross section of their daughters. Thus, the study of resonances can provide an independent probe of the time evolution of the source from chemical to kinetic freeze-out and detailed information on hadronic interaction at later stages. This has been measured in Au+Au and compared to that in p+p for the K^*, Σ^*, and Λ^* [4,7] resonances. Now, with the addition of the d+Au measurement, we can gain insight into the rescattering processes in p+p and Au+Au collisions.

In this paper, we present the first measurements of $\rho(770)^0$, $K^*(892)$, $\Delta(1232)^{++}$, $\Sigma(1385)$, and $\Lambda(1520)$ in d+Au collisions at $\sqrt{s_{NN}} = 200$ GeV at RHIC reconstructed via their hadronic decay channels using the solenoidal tracker at RHIC (STAR) detector. The $\rho(770)^0$, $K^*(892)$, $\Delta(1232)^{++}$, and $\Sigma(1385)$ masses are presented as a function of p_T in d+Au collisions and the ρ^0 and Δ^{++} masses are compared with the measurements in p+p collisions. The p_T spectra of these resonances are presented for different centralities in d+Au collisions. The $\langle p_T \rangle$ of resonances measured in minimum bias collisions are compared with the $\langle p_T \rangle$ of π, K, and $\bar{p}$. The ρ^0/π^-, K^*/K^-, Δ^{++}/p, $\Sigma(1385)/\Lambda$, and $\Lambda(1520)/\Lambda$ ratios in d+Au and minimum bias p+p collisions are compared. The nuclear modification factors $R_{d\mathrm{Au}}$ of these resonances are compared to the $R_{d\mathrm{Au}}$ of charged hadrons and the Cronin (initial state multiple scattering) enhancement [19] is discussed.

II. EXPERIMENT

We present measurements of resonances via their hadronic decay channels (see Table I) in d+Au collisions at $\sqrt{s_{NN}} =$ 200 GeV using the time projection chamber (TPC) [20], which is the primary tracking device of the STAR experiment.

A minimum bias trigger was defined by requiring that at least one beam-rapidity neutron impinges on the zero degree calorimeter (ZDC) [21] in the Au beam direction. The measured minimum bias cross section amounts to 95% $\pm$ 3% of the total d+Au geometric cross section. Charged particle multiplicity within the pseudorapidity interval $-3.8 < \eta < -2.8$ was measured in a forward TPC (FTPC) [22] in the Au beam direction and served as the basis of our d+Au centrality tagging scheme, as described elsewhere [23]. The d+Au centrality definition consists of three event centrality classes: 0–20%, 20–40%, and 40–100% of the total d+Au cross section [24]. The analysis of different centralities was restricted to events with a primary vertex within 50 cm of the

TABLE I. Resonances measured in d+Au collisions, their corresponding hadronic decay channels, branching ratios, and lifetimes [26].

Resonance	Decay channel	B.R.	$c\tau$ (fm)
$\rho^0(770)$	$\pi^+\pi^-$	~100%	1.3
$K^*(892)^0$	$K^+\pi^-$	~66.7%	3.9
$\bar{K}^*(892)^0$	$K^-\pi^+$	~66.7%	4
$K^*(892)^{\pm}$	$K^0_S\pi^{\pm}$	~66.7%	4
$\Delta(1232)^{++}$	$p\pi^+$	~100%	1.6
$\bar{\Delta}(1232)^{--}$	$\bar{p}\pi^-$	~100%	1.6
$\Sigma(1385)^+$	$\Lambda\pi^+$	~87%	5.5
$\bar{\Sigma}(1385)^-$	$\bar{\Lambda}\pi^-$	~87%	5.5
$\Sigma(1385)^-$	$\Lambda\pi^-$	~87%	5.0
$\bar{\Sigma}(1385)^+$	$\bar{\Lambda}\pi^+$	~87%	5.0
$\Lambda(1520)$	pK^-	~22.5%	12.6
$\bar{\Lambda}(1520)$	$\bar{p}K^+$	~22.5%	12.6

TABLE II. Data set for each centrality used in the analysis of resonances in d+Au collisions.

Centrality	Number of events	Primary vertex (cm)	Resonance
Minimum bias	$\sim 16 \times 10^6$	± 100	ρ^0, Σ^*
Minimum bias	$\sim 15 \times 10^6$	± 75	K^*
Minimum bias	$\sim 14 \times 10^6$	± 70	Λ^*
Minimum bias	$\sim 11.6 \times 10^6$	± 50	Δ^{++}

center of the TPC along the beam direction to ensure uniform acceptance in the η range studied. For the minimum bias events, the FTPC was not used, so events with a primary vertex within 100 cm were accepted, still maintaining a uniform acceptance in the η range studied. To improve the statistics in the case of the $K^*(892)$, events with a primary vertex within 75 cm were accepted for the centrality studies. The difference between using 50 and 75 cm as the primary vertex cut was taken into account in the systematic errors. The same primary vertex cut was used for the minimum bias events. To improve statistics in the case of the $\Lambda(1520)$, events with a primary vertex within 70 cm were accepted for centrality selected minimum bias events. A summary of the relevant data sets is given in Table II.

We also present measurements in p+p collisions of the Δ^{++} where a minimum bias trigger was defined using coincidences between two beam-beam counters that measure the charged particle multiplicity at forward pseudorapidities ($3.3 < |\eta| < 5.0$). In this case, $\sim 6 \times 10^6$ events were used, where only events with a primary vertex within ± 50 cm were accepted.

In addition to momentum information, the TPC provides particle identification for charged particles by measuring their ionization energy loss (dE/dx). Figure 1 shows dE/dx as a function of momentum p measured in the TPC. The different bands presented in Fig. 1 represent Bichsel distributions folded with the experimental resolutions and correspond to different particle species [25]. Charged pions and kaons can be separated in momenta up to about 0.75 GeV/c, while

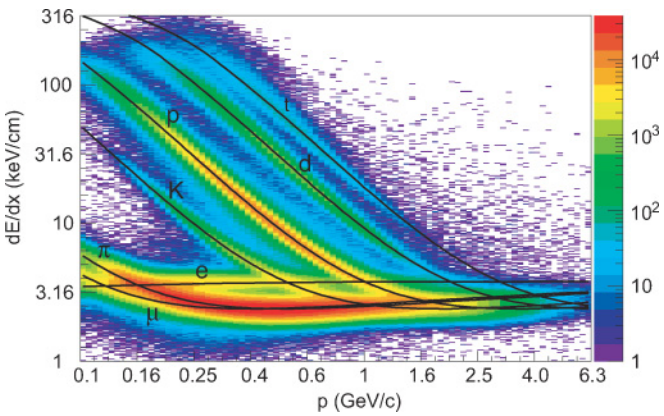

FIG. 1. (Color online) dE/dx for charged particles vs momentum measured by the TPC in d+Au collisions. The curves are the Bichsel function [25] for different particle species.

(anti-)protons can be identified for momenta of up to about 1.1 GeV/c. In Fig. 1, the Bichsel function [25] is used instead of the traditional Bethe-Bloch parametrization [26] in order to improve particle identification. To quantitatively describe the particle identification, the variable $N_{\sigma\pi}$, which expresses energy loss in the units of the standard deviation of a Gaussian formed by the logarithm of truncated energy loss, is defined (in this case for pions) as

$$N_{\sigma\pi} = \frac{1}{\sigma_{dE/dx}(L_{\mathrm{TPC}})} \log \frac{dE/dx_{\mathrm{measured}}}{\langle dE/dx \rangle_{\pi}}, \tag{1}$$

where $dE/dx_{\mathrm{measured}}$ is the measured energy loss for a track, $\langle dE/dx \rangle_{\pi}$ is the expected mean energy loss for charged pions with a given momentum, and $\sigma_{dE/dx}(L_{\mathrm{TPC}})$ is the dE/dx resolution that depends on the track length in the TPC that is used in the dE/dx measurement. For L_{TPC} equal to 72 cm, corresponding to a 90° angle with the beam axis, the resolution is 8.1%. In the case of charged kaon and charged proton identification, similar definitions of $N_{\sigma K}$ and $N_{\sigma p}$ can be obtained. To quantitatively select the charged pions, kaons, and protons, specific analysis cuts (described later) are then applied to the variables $N_{\sigma\pi}$, $N_{\sigma K}$, and $N_{\sigma p}$.

III. PARTICLE SELECTION

In all cases, particles and antiparticles are combined to improve the statistics. In the following, the term K^{*0} stands for K^{*0} or $\bar{K}^{*0}$, and the term K^* stands for K^{*0}, $\bar{K}^{*0}$, or $K^{*\pm}$, unless otherwise specified. The term Δ^{++} stands for Δ^{++} or $\bar{\Delta}^{--}$, the term Σ^* stands for $\Sigma(1385)^+$, $\Sigma(1385)^-$, $\bar{\Sigma}(1385)^-$, or $\bar{\Sigma}(1385)^+$, and the term Λ^* stands for $\Lambda(1520)$ or $\bar{\Lambda}(1520)$, unless otherwise specified.

As these studied resonances decay in such short times that the daughters seem to originate from the interaction point, only the charged pion, kaon, and proton candidates whose distance of closest approach to the primary interaction vertex was less than 3 cm were selected. Such candidate tracks are referred to as primary tracks. To avoid the acceptance drop in the high η range, all track candidates were required to have $|\eta| < 0.8$. For all candidates, to avoid selecting split tracks, a cut on the ratio of the number of TPC track fit points and the maximum possible points was required. In addition, a minimum p_T cut was applied to maintain reasonable momentum resolution.

In the case of the ρ^0, a series of cuts was applied to the charged pion candidates to ensure track fit quality and good dE/dx resolution. A compilation of the cuts used in the ρ^0 analysis is given in Table III, and the ρ^0 correction factor (reconstruction efficiency multiplied by the detector acceptance) as a function of invariant mass for a particular p_T bin is depicted in Fig. 2. In general, the correction factor increases as a function of transverse momentum. The fact that the correction factor is larger at low values of $M_{\pi\pi}$ and larger values of p_T is simply due to kinematics. In the case of wide resonances, such as the ρ^0 and Δ^{++}, the correction factor depends on the invariant mass for each p_T interval that is being analyzed. In this case, the correction is applied as a function

TABLE III. Track cuts for charged kaons and charged pions and topological cuts for neutral kaons used in the ρ^0 and K^* analyses in d+Au collisions. *decayLength* is the decay length, *dcaDaughters* is the distance of closest approach between the daughters, $dcaV0PrmVx$ is the distance of closest approach between the reconstructed K^0_S momentum vector and the primary interaction vertex, *dcaPosPrmVx* is the distance of closest approach between the positively charged granddaughter and the primary vertex, *dcaNegPrmVx* is the distance of closest approach between the negatively charged granddaughter and the primary vertex, $M_{K^0_S}$ is the K^0_S invariant mass in GeV/c^2, *NFitPnts* is the number of fit points of a track in the TPC, *NTpcHits* is the number of hits of a track in the TPC, *MaxPnts* is the number of maximum possible points of a track in the TPC, and *DCA* is the distance of closest approach to the primary interaction point. The normalization region corresponds to the interval in which the invariant mass and the background reference distributions are normalized.

Cuts	ρ^0	K^{*0}	$K^{*\pm}$	
			Daughter $\pi^\pm$	K^0_S
$N_{\sigma K}$		(−2.0, 2.0)		*decayLength* > 2.0 cm
$N_{\sigma\pi}$	(−3.0, 3.0)	(−3.0, 3.0)	(−2.0, 2.0)	*dcaDaughters* < 1.0 cm
Kaon p (GeV/c)	>0.2	(0.2, 0.7)		$itdcaV0PrmVx$ < 1.0 cm
Kaon p_T(GeV/c)	>0.2	(0.2, 0.7)		*dcaPosPrmVx* > 0.5 cm
Pion p(GeV/c)	>0.2	(0.2, 10.0)	(0.2, 10.0)	*dcaNegPrmVx* > 0.5 cm
Pion p_T (GeV/c)	>0.2	(0.2, 10.0)	(0.2, 10.0)	$M_{K^0_S}$ (GeV/c^2): (0.48, 0.51)
NFitPnts	>15	>15	>15	π^+: $NTpcHits$ > 15
NFitPnts/*MaxPnts*	>0.55	>0.55	>0.55	π^-: $NTpcHits$ > 15
Kaon and pion η	$\lvert\eta\rvert$ < 0.8	$\lvert\eta\rvert$ < 0.8	$\lvert\eta\rvert$ < 0.8	π^+ : p > 0.2 GeV/c
DCA (cm)	<3.0	<3.0	<3.0	π^-: p > 0.2 GeV/c
Mass normalization region (GeV/c^2)	(1.5, 2.5)			
Pair y	$\lvert y\rvert$ < 0.5	$\lvert y\rvert$ < 0.5	$\lvert y\rvert$ < 1.0	

of the invariant mass for each p_T bin. In the case of narrow resonances, such as the K^*, Σ^*, and Λ^*, the correction factor is dependent only on the p_T bin being analyzed. Therefore, the correction is performed as a function of p_T only.

For the K^* analysis, charged kaon candidates were selected by requiring $|N_{\sigma K}| < 2$, while a looser cut $|N_{\sigma\pi}| < 3$ was applied to select the charged pion candidates to maximize statistics for the K^* analysis. Such N_σ cuts do not unambiguously select kaons and pions, but do help to reduce the background significantly. The background was reduced further

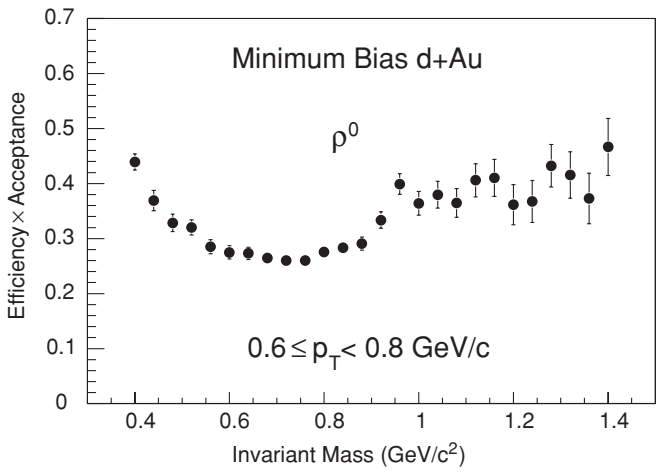

FIG. 2. ρ^0 reconstruction efficiency×detector acceptance as a function of the invariant mass for minimum bias d+Au. The error shown is due to the available statistics in the simulation.

by selecting only kaon candidates with $p < 0.7$ GeV/c. This momentum cut ensures clearer identification by minimizing contamination from misidentified correlated pairs and thus the systematic uncertainties [4]. The $K^{*\pm}$ first undergoes a strong decay to produce a K^0_S and a charged pion hereafter labeled as the $K^{*\pm}$ daughter pion. Then, the produced K^0_S decays weakly into a $\pi^+\pi^-$ pair with $c\tau = 2.67$ cm. The oppositely charged pions from the K^0_S decay are called the $K^{*\pm}$ granddaughter pions. The charged daughter pion candidates were selected from primary track samples, and the K^0_S candidates were selected through their decay topology [27,28]. The procedure is briefly outlined below. The granddaughter charged pion candidates were selected from tracks that do not originate from the primary collision vertex. Oppositely charged candidates were then paired to form neutral decay vertices. When the K^0_S candidate was paired with the daughter pion to reconstruct the charged K^*, tracks were checked to avoid double counting among the three tracks used. Cuts were applied to the daughter and granddaughter candidates to ensure track fit quality and good dE/dx resolution and to reduce the combinatorial background in the K^0_S invariant mass distribution. All the cuts used in this K^* analysis are summarized in Table III and the K^* reconstruction correction factors are shown in Fig. 3.

The cuts applied to the Δ^{++} and Λ^* decay daughters were the same as described above for the ρ^0 and K^{*0}, and their respective values are given in Table IV. We also present the Δ^{++} measured in p+p collisions, and the cuts and their respective values applied to the decay daughters are the same as the ones used in the d+Au analysis and shown in Table IV. Similarly to the $K^{*\pm}$, the $\Sigma^{*\pm}$ first undergoes a strong decay to produce a Λ, which subsequently decays weakly into

TABLE IV. Track cuts for charged kaons, charged pions, and charged protons and topological cuts for lambdas used in the Δ^{++}, Λ^*, and $\Sigma^{*\pm}$ analyses in d+Au collisions. *decayLength* is the decay length, *dcaDaughters* is the distance of closest approach between the daughters, $dcaV0PrmVx$ is the distance of closest approach between the reconstructed Λ momentum vector and the primary interaction vertex, *dcaPosPrmVx* is the distance of closest approach between the positively charged granddaughter and the primary vertex, *dcaNegPrmVx* is the distance of closest approach between the negatively charged granddaughter and the primary vertex, M_Λ is the Λ invariant mass in GeV/c^2, $NFitPnts$ is the number of fit points of a track in the TPC, *NTpcHits* is the number of hits of a track in the TPC, *MaxPnts* is the number of maximum possible points of a track in the TPC, θ^* is the angle in the center-of-mass of one decay particle with respect to the mother particle, and *DCA* is the distance of closest approach to the primary interaction point. The normalization region corresponds to the interval in which the invariant mass and the background reference distributions are normalized.

Cuts	Δ^{++}	Λ^*	$\Sigma^{*\pm}$	
			Daughter $\pi^\pm$	Λ
$N_{\sigma K}$		$(-2.0, 2.5)$		
$N_{\sigma p}$	$(-2.0, 2.0)$	$(-2.0, 2.5)$		*decayLength* (cm): (5.0,30.0)
$N_{\sigma\pi}$	$(-2.0, 2.0)$		$(-3.0, 3.0)$	$dcaDaughters < 1.0$ cm
Kaon p (GeV/c)		(0.2, 0.8)		
Kaon p_T (GeV/c)				
Proton p (GeV/c)	(0.3, 1.1)	(0.2, 1.0)		$dcaV0PrmVx < 1.1$ cm
Proton p_T (GeV/c)	(0.3, 1.1)			$dcaPosPrmVx > 0.9$ cm
Pion p (GeV/c)	(0.1, 0.6)		(0.15, 1.5)	$dcaNegPrmVx > 2.5$ cm
Pion p_T (GeV/c)	(0.1, 0.6)			M_Λ (GeV/c^2): (1.11, 1.12)
	Proton p >Pion p			
NFitPnts	>15	>20	>15	p: $NTpcHits > 15$
NFitPnts/*MaxPnts*	>0.55	>0.51	>0.55	π^- : $NTpcHits > 15$
Proton and pion η	$\lvert\eta\rvert < 0.8$		$\lvert\eta\rvert < 1.5$	p: $p > 0.1$ GeV/c
DCA (cm)	<3.0	<1.5	<1.5	π^-: $p > 0.1$ GeV/c
$\cos\theta^*$		$(-0.8, 0.8)$		
Mass Normalization Region (GeV/c^2)	See text	(1.55–1.8)	(1.45–2.0)	
Pair y	$\lvert y\rvert < 0.5$	$\lvert y\rvert < 0.5$	$\lvert y\rvert < 0.75$	

$\pi^- p$ with a $c\tau = 7.89$ cm. The cuts applied to the $\Sigma^{*\pm}$ decay daughters and granddaughters are the same as mentioned for the $K^{*\pm}$, and the values are shown in Table IV. The Δ^{++}, Λ^*, and $\Sigma^{*\pm}$ reconstruction correction factors are shown in Figs. 4, 5, and 6, respectively.

IV. ANALYSIS AND RESULTS

The ρ^0 measurement was performed by calculating the invariant mass for each $\pi^+\pi^-$ pair in an event which passed the cuts. The resulting invariant mass distribution was then compared with a reference distribution calculated from the

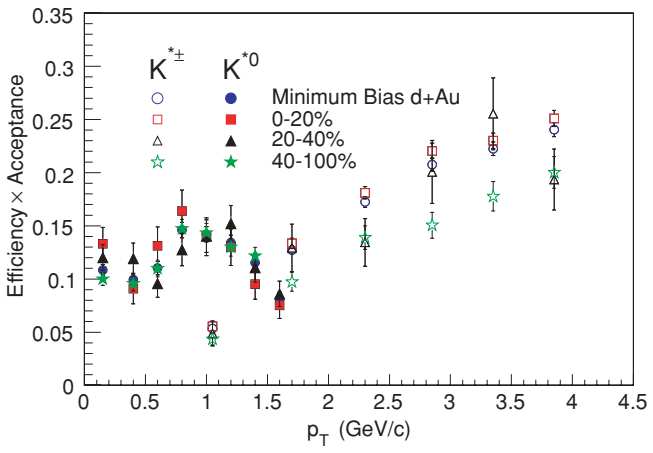

FIG. 3. (Color online) K^{*0} and $K^\pm$ reconstruction efficiency×detector acceptance as a function of p_T for minimum bias d+Au and three different centralities.

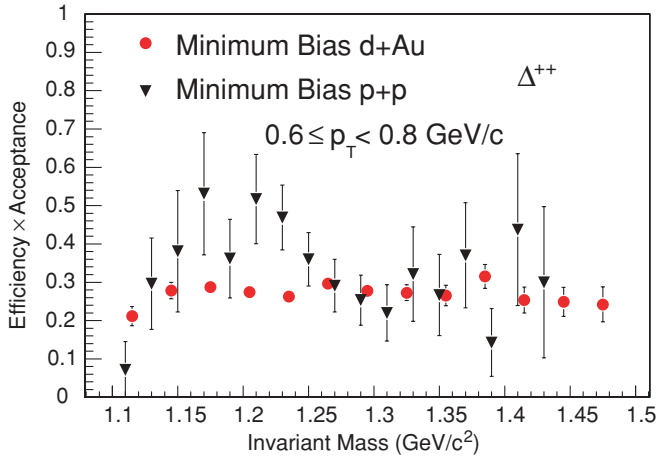

FIG. 4. (Color online) Δ^{++} reconstruction efficiency×detector acceptance as a function of the invariant mass for minimum bias d+Au and p+p. The error shown is due to the available statistics in the simulation.

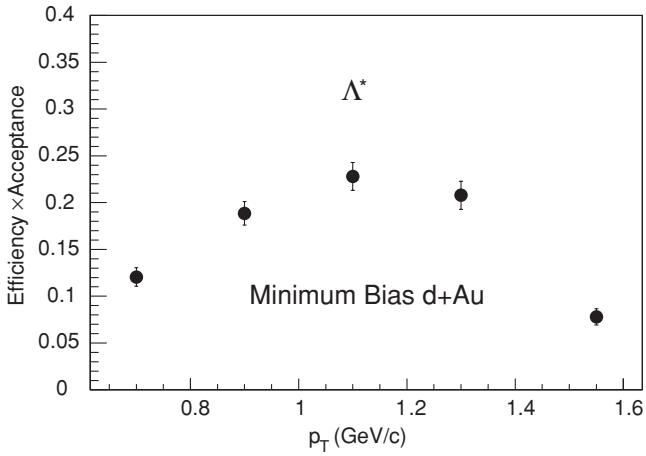

FIG. 5. Λ^* reconstruction efficiency×detector acceptance as a function of p_T for minimum bias d+Au. The error shown is due to the available statistics in the simulation.

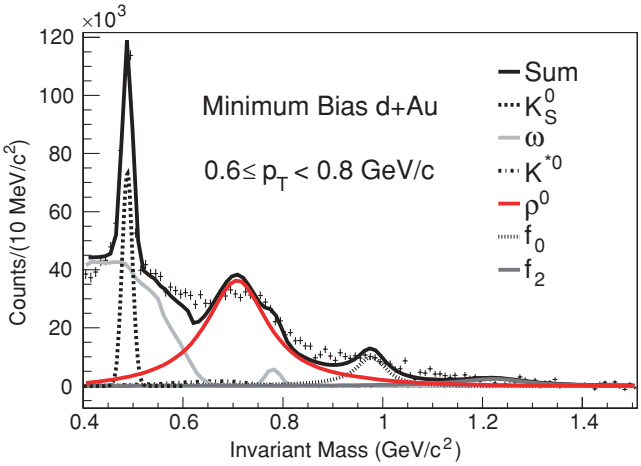

FIG. 7. (Color online) Raw $\pi^+\pi^-$ invariant mass distribution at midrapidity after subtraction of the like-sign reference distribution for minimum bias d+Au collisions with the hadronic cocktail fit.

geometric mean of the invariant mass distributions obtained from uncorrelated like-sign pion pairs from the same events [4]. The $\pi^+\pi^-$ invariant mass distribution $M_{\pi\pi}$ and the like-sign reference distribution were normalized to each other between $1.5 \leqslant M_{\pi\pi} \leqslant 2.5$ GeV/c^2.

The K^*, Δ^{++}, Σ^*, and Λ^* measurements were performed using the mixed-event technique [4], in which the reference background distribution is built with uncorrelated unlike-sign kaons and pions, protons and pions, lambdas and pions, and protons and kaons from different events, respectively. The background is normalized over a wide kinematic range (see Tables III and IV) and then subtracted from the corresponding invariant mass distribution.

A. Masses and widths

The mass and width of resonances have been of great interest because of their possible modification in the medium

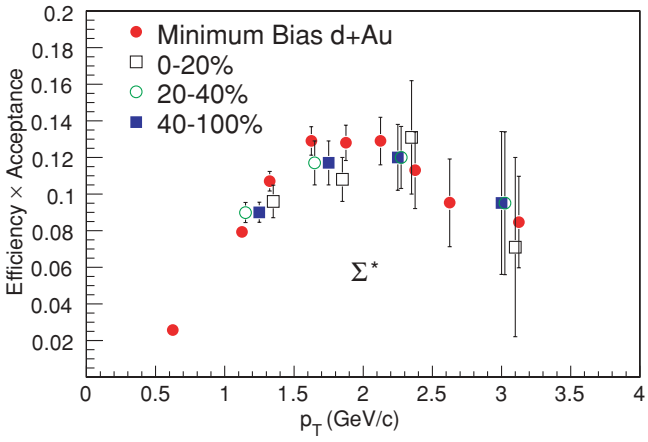

FIG. 6. (Color online) $\Sigma^{*\pm}$ reconstruction efficiency×detector acceptance as a function of p_T for minimum bias d+Au and three different centralities. The error shown is due to the available statistics in the simulation.

produced in heavy-ion collisions [18]. It is interesting to study how the resonance masses and widths behave in d+Au collisions.

The corresponding $\pi^+\pi^-$ raw invariant mass distribution after the like-sign background subtraction for minimum bias d+Au collisions at midrapidity ($|y| < 0.5$) for a particular p_T bin is shown in Fig. 7. The solid black line in Fig. 7 is the sum of all the well-defined contributions to the $M_{\pi\pi}$ distribution (hadronic cocktail) [3]. The K^0_S was fit with a Gaussian function. The ω and $K^*(892)^0$ shapes were obtained from the HIJING event generator [29], with the kaon being misidentified as a pion in the case of the K^{*0}. The $\rho^0(770)$, $f_0(980)$, and $f_2(1270)$ were fit to a BW×PS function, where BW is the relativistic Breit-Wigner function [30]

$$\mathrm{BW} = \frac{M_{\pi\pi} M_0 \Gamma}{\left(M_0^2 - M_{\pi\pi}^2\right)^2 + M_0^2 \Gamma^2}, \tag{2}$$

and PS is the Boltzmann factor [15,16,31,32]

$$\mathrm{PS} = \frac{M_{\pi\pi}}{\sqrt{M_{\pi\pi}^2 + p_T^2}} \times \exp\left(-\frac{\sqrt{M_{\pi\pi}^2 + p_T^2}}{T}\right), \tag{3}$$

to account for phase space. Here, T is the temperature parameter at which the resonance is emitted [16], and

$$\Gamma = \Gamma_0 \times \frac{M_0}{M_{\pi\pi}} \times \left(\frac{M_{\pi\pi}^2 - 4m_\pi^2}{M_0^2 - 4m_\pi^2}\right)^{(2\ell+1)/2} \tag{4}$$

is the width [30], which changes as a function of momentum due to reconstruction effects. Here, M_0 and ℓ are the resonance mass and spin, respectively. The masses of K^0_S, ρ^0, f_0, and f_2 were free parameters in the fit, and the widths of f_0 and f_2 were fixed according to Ref. [26]. The uncorrected yields of K^0_S, ρ^0, ω, f_0, and f_2 were free parameters in the fit, while the K^{*0} fraction was fixed according to the $K^*(892)^0 \rightarrow \pi K$ measurement, where the amount of contamination was determined using a detailed simulation of the TPC response using GEANT [33]. The ρ^0, ω, K^{*0}, f_0, and f_2 distributions

were corrected for the detector acceptance and efficiency determined from simulation. The signal-to-background ratio before subtraction is about 1/100.

The cocktail fit does not reproduce the $\pi^+\pi^-$ raw invariant mass distribution at ~600 and ~850 MeV/c^2, respectively. This is understood to be due to other contributions to the hadronic cocktail aside from what was described above, e.g., the $f_0(600)$, which is not very well established [26]. The ω yield in the hadronic cocktail fits may account for some of these contributions and may cause the apparent decrease in the ρ^0/ω ratio between minimum bias $p+p$ and peripheral Au+Au interactions.

The ρ^0 mass is shown as a function of p_T in Fig. 8 for minimum bias d+Au interactions and 0–20%, 20–40%, and 40–100% of the total d+Au cross section. A mass shift of ~50 MeV/c^2 is observed at low p_T. The ρ^0 width was fixed at $\Gamma_0 = 160$ MeV/c^2, consistent with folding the ρ^0 natural width (150.9 ± 2.0 MeV/c^2 [26]) with the intrinsic resolution of the detector [$\delta p_T/p_T = 0.005(1 + p_T)$ [33].

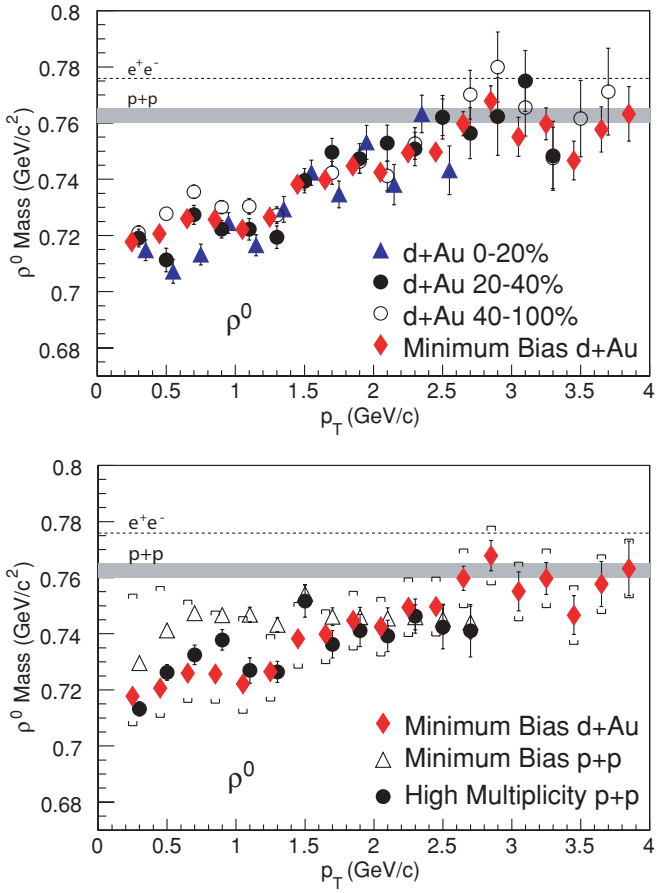

FIG. 8. (Color online) ρ^0 mass as a function of p_T at $|y| < 0.5$ for minimum bias d+Au interactions and 0–20%, 20–40%, and 40–100% of the total d+Au cross section (upper panel). The errors shown are statistical only. The comparison of the ρ^0 mass as a function of p_T at $|y| < 0.5$ measured in minimum bias d+Au, $p+p$, and high multiplicity $p+p$ [3] interactions (lower panel). The brackets indicate the systematic uncertainty ,and it is shown only for the minimum bias d+Au measurement for clarity. The diamonds have been shifted to lower values on the abscissa by 100 MeV/c in p_T for clarity.

The temperature parameter used in the PS factor was $T = 160$ MeV, which was also used in the $p+p$ analysis [3]. In Fig. 8, only the systematic uncertainty for the minimum bias d+Au measurement is depicted for clarity. However, the systematic uncertainty for the other d+Au centrality measurements are similar, if not less than the systematic uncertainty for the minimum bias d+Au measurement.

The ρ^0 mass at $|y| < 0.5$ for minimum bias and three different centralities in d+Au collisions at $\sqrt{s_{NN}} = 200$ GeV increases as a function of p_T and is systematically lower than the value reported by NA27 at CERN-LEBC-EHS [34]. This experiment measured the ρ^0 in minimum bias $p+p$ collisions at $\sqrt{s} = 27.5$ GeV for $x_F > 0$, where x_F is the ratio between the longitudinal momentum and the maximum momentum of the meson. In Fig. 8, the shaded areas indicate the ρ^0 mass measured in $p+p$ collisions (762.6 ± 2.6 MeV/c^2) by NA27 [34] and the dashed lines represent the average of the ρ^0 mass measured in e^+e^- (775.6 ± 0.5 MeV/c^2) [26]. The ρ^0 mass measured in 0–20% of the total d+Au cross section is slightly lower than the mass measured in the most peripheral centrality class. The masses measured in minimum bias d+Au, $p+p$ [3], and high multiplicity $p+p$ [3] interactions are compared in Fig. 8. The comparison shows that the ρ^0 mass measured in minimum bias d+Au and high multiplicity $p+p$ interactions are comparable. A mass shift of ~70 MeV/c^2 was also measured in Au+Au collisions [3]. Dynamical interactions with the surrounding matter, interference between various $\pi^+\pi^-$ scattering channels, phase-space distortions due to the rescattering of pions forming ρ^0, and Bose-Einstein correlations between ρ^0 decay daughters and pions in the surrounding matter were previously given as the possible explanations [3]. It has been proposed [35] that the mass shift observed in $p+p$ collisions is due to $\pi\pi$ rescattering, which requires no medium. Since one also does not expect a medium to be formed in d+Au collisions, if dynamical interactions are also the explanation for the mass shift, then the rescattering of the ρ^0 with the surrounding particles must exist. We also observe that the ρ^0 mass is not modified at high p_T.

NA27 measured the ρ^0 in minimum bias $p+p$ at $\sqrt{s} = 27.5$ GeV for $x_F > 0$ and reported a mass of 762.6 ± 2.6 MeV/c^2 [34]. The invariant $\pi^+\pi^-$ mass distribution after subtraction of the mixed-event reference distribution is shown in Fig. 9. The vertical dash-dotted line represents the average of the ρ^0 mass 775.8 ± 0.5 MeV/c^2 measured in e^+e^- collisions [26]. The vertical dashed line, which accounts for the phase space, is the ρ^0 mass reported by NA27 (762.6 ± 2.6 MeV/c^2) [34]. As shown in Fig. 9, the position of the ρ^0 peak is shifted by ~30 MeV/c^2 compared to the ρ^0 mass in the vacuum 775.8 ± 0.5 MeV/c^2 [26].

NA27 obtained the ρ^0 mass by fitting the invariant $\pi^+\pi^-$ mass distribution by the (BW × PS + BG) function, where in this analysis, the phase-space function used is the same as the combinatorial background (BG). NA27 reported a mass of 762.6 ± 2.6 MeV/c^2, which is ~10 MeV/c^2 lower than the ρ^0 mass in the vacuum. Ideally, the PS factor should have accounted for the shift on the ρ^0 peak, and the mass obtained from the fit should have agreed with the ρ^0 mass in the vacuum. However, just like in the STAR measurement, this was not the

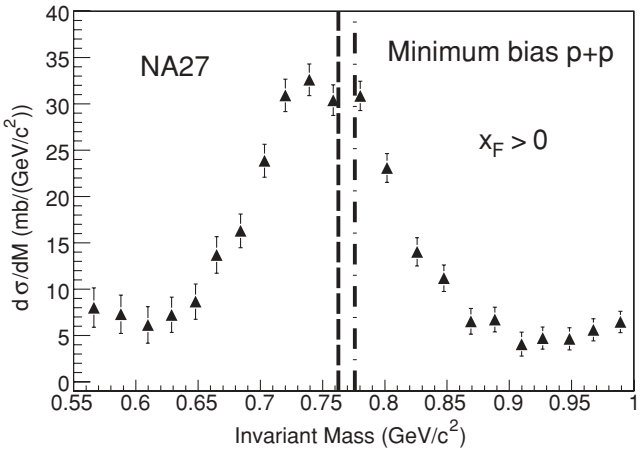

FIG. 9. Invariant $\pi^+\pi^-$ mass distribution after background subtraction for minimum bias p+p collisions measured by NA27. For details, see Ref. [34]. The vertical dash-dotted line represents the average of the ρ^0 mass 775.8 ± 0.5 MeV/c^2 measured in e^+e^- [26]. The vertical dashed line is the ρ^0 mass 762.6 ± 2.6 MeV/c^2 reported by NA27 [34].

case, since the phase space did not account for the mass shift on the position of the ρ^0 peak.

At the CERN-LEP accelerator, OPAL, ALEPH, and DELPHI experiments measured the ρ^0 in inclusive e^+e^- reactions at $\sqrt{s} = 90$ GeV [36–39]. OPAL reported a shift in the position of the ρ^0 peak by ∼70 MeV/c^2 at low x_p, where x_p is the ratio between the meson and the beam energies, and no shift at high $x_p (x_p \sim 1)$ [36,37]. OPAL also reported a shift in the position of the $\rho^\pm$ peak from −10 to −30 MeV/c^2, which was consistent with the ρ^0 measurement [38]. ALEPH reported the same shift on the position of ρ^0 peak as observed by OPAL [39]. DELPHI fit the raw invariant $\pi^+\pi^-$ mass distribution to the (BW × PS + BG) for $x_p > 0.05$ and reported a ρ^0 mass of 757 ± 2 MeV/c^2 [40], which is 7.5 standard deviations below the ρ^0 mass in the vacuum (775.8 ± 0.5 MeV/c^2). As one can see, similar to NA27, DELPHI assumed that the phase space was described by the background function. Bose-Einstein correlations were used to describe the shift on the position of ρ^0 peak. However, high chaoticity parameters ($\lambda \sim 2.5$) were needed [36,37,39]. Previous measurements of the ρ mass shift and possible explanations are discussed elsewhere [3]. The masses of the ρ^0 and other short-lived resonances in the vacuum are obtained only in exclusive reactions and not in inclusive reactions where many particles are produced.

As previously mentioned [3], one uncertainty in the hadronic cocktail fit depicted in Fig. 7 is the possible existence of correlations of unknown origin near the ρ^0 mass. An example is correlations in the invariant mass distribution from particles such as the $f_0(600)$ which are not well established [26]. The ω yield in the hadronic cocktail fits may account for some of these contributions. To evaluate the systematic uncertainty in the ρ^0 mass due to poorly known contributions in the hadronic cocktail, the ρ^0 mass was obtained by fitting the peak to the BW×PS function plus an exponential function representing these contributions. Using this procedure, the ρ^0 mass is systematically higher than the mass obtained from the

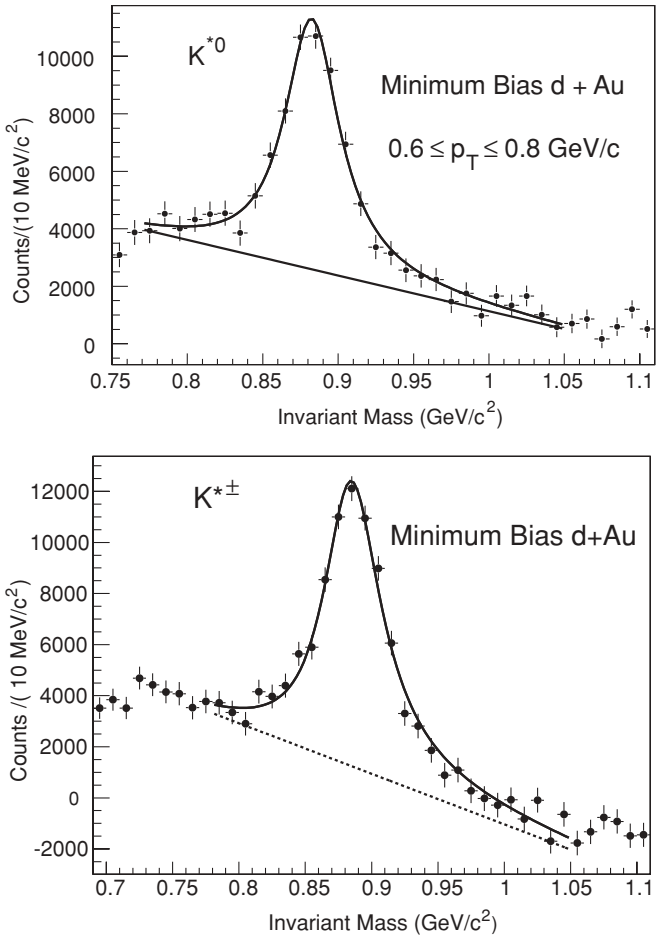

FIG. 10. Mixed-event background subtracted $K\pi$ raw invariant mass distribution for a particular K^{*0} p_T bin (upper panel) and the mixed-event background subtracted $K^0_S\pi^\pm$ raw invariant mass distribution integrated over the $K^{*\pm}$ p_T (lower panel) at $|y| < 0.5$ for minimum bias d+Au interactions. The dashed lines are the linear function that describes the residual background.

hadronic cocktail fit. This uncertainty is the main contribution to the systematic uncertainties shown in Fig. 8, and it can be as large as ∼35 MeV/c^2 for low p_T. Other contributions to the systematic errors shown in Fig. 8 result from uncertainty in the measurement of particle momenta of ∼3 MeV/c^2 and from the hadronic cocktail fits themselves of ∼10 MeV/c^2. The systematic uncertainties are common to all p_T bins and are correlated between all centralities in the d+Au measurements.

Figure 10 depicts the mixed-event background subtracted $K\pi$ and $K^0_S\pi^\pm$ invariant mass distributions for minimum bias d+Au interactions at midrapidity for a particular p_T interval of the K^{*0} p_T and integrated over the full measured p_T range of the $K^{*\pm}$. The signal-to-background ratio before subtraction is 1/50 for both cases. The solid black line corresponds to the fit to the relativistic p-wave Breit-Wigner function multiplied by the phase space [Eq. (2)], with $T = 160$ MeV, plus a linear function that represents the residual background. This comes predominantly from correlated $K\pi$ pairs and correlated but misidentified pairs. A detailed study has been presented previously [4].

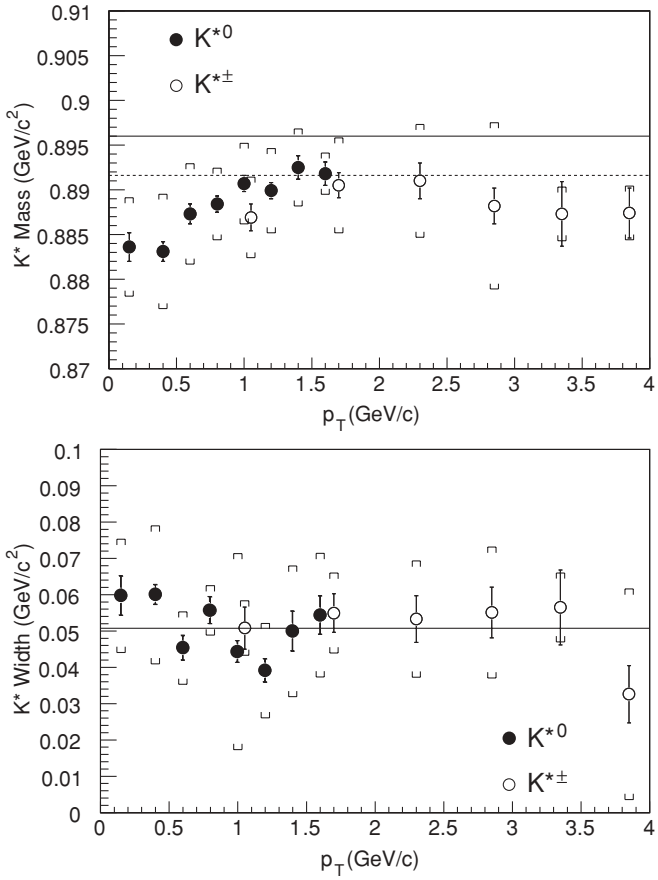

FIG. 11. K^* mass (upper panel) and width (lower panel) as a function of p_T at $|y| < 0.5$ for minimum bias d+Au collisions. In the upper panel, the solid line is the PDG K^{*0} mass (0.8961 GeV/c^2) [26]. The dashed line is the PDG $K^{*\pm}$ mass (0.8917 GeV/c^2) [26]. In the lower panel, the solid line is the K^{*0} and $K^{*\pm}$ widths (0.0507 GeV/c^2) [26]. The brackets indicate the systematic uncertainties.

The K^* masses and widths at $|y| < 0.5$ for minimum bias d+Au interactions as a function of p_T are depicted in Fig. 11. Both mass and width were obtained by correcting the K^* distribution for detector acceptance and efficiency that was determined from a detailed simulation of the TPC response using GEANT [33]. The K^{*0} mass increases as a function of p_T, and at low p_T ($p_T < 1.1$ GeV/c) the mass is significantly smaller than previously reported values [26]. A similar mass shift was observed in minimum bias p+p collisions at $\sqrt{s_{NN}} = 200$ GeV [4], and the possible explanations are the same as described for the ρ^0 meson. Even though a K^{*0} mass shift in d+Au collisions has not been observed before, it is important to note that previous measurements were mainly interested in extracting the resonance cross section [34]. In addition, we observe a mass shift at low p_T of $\sim$10 MeV/c^2, while previous analyses only presented the K^{*0} mass integrated in p_T, x_F, or x_p. The $K^{*\pm}$ mass is in agreement with previous values within errors [26]. However, this could be due to the limited p_T range covered. There is no significant difference between the measured K^* width and the previous values [26].

The main contributions to the systematic uncertainties on the K^* mass and width were evaluated as a function of p_T using a different residual background function (second-order polynomial), different fitting functions to the K^* invariant mass (nonrelativistic BW, relativistic BW without phase-space factor), and different slope parameters in the BW×PS function (140 and 180 MeV). In addition, the mass and width were obtained separately for K^{*0}, $\bar{K}^{*0}$, K^{*+}, and K^{*-}. The systematic uncertainty due to detector effects was also accounted for. The systematic uncertainty can be as large as $\sim$6.5 (9.5) MeV/c^2 and $\sim$25 (30) MeV/c^2 for the $K^{*0}(K^{*\pm})$ mass and width, respectively.

The $p\pi$ raw invariant mass distributions after the mixed-event background subtraction for minimum bias d+Au and p+p interactions at midrapidity for a particular p_T bin are shown in Fig. 12. Before background subtractions, the signal-to-background ratios are 1/50 and 1/30 for minimum bias d+Au and p+p interactions, respectively. The solid black line corresponds to the fit to a relativistic p-wave Breit-Wigner function multiplied by the phase space, with $T = 160$ MeV, plus a Gaussian function that represents the

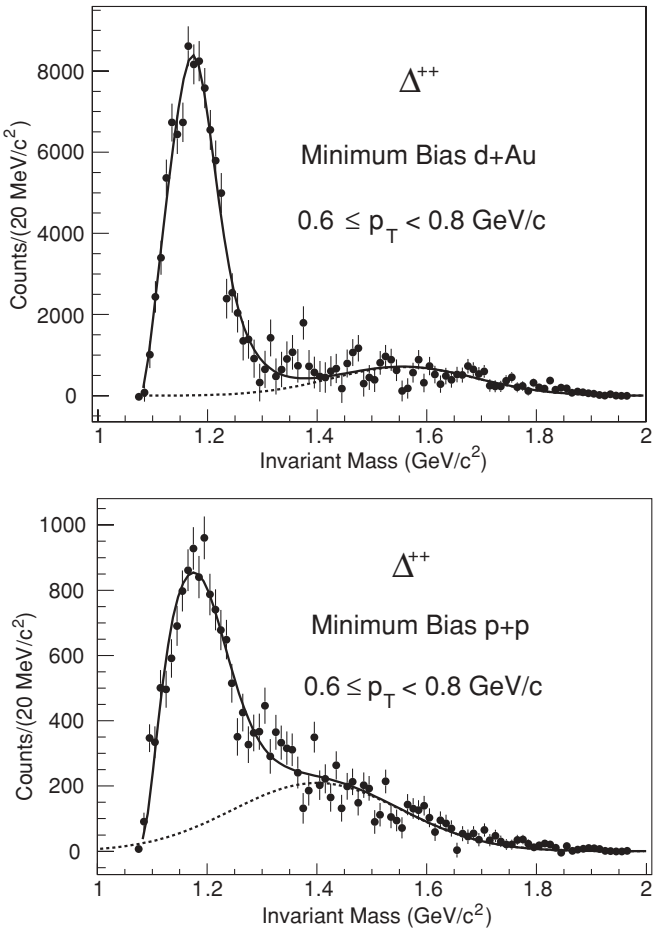

FIG. 12. Mixed-event background subtracted $p\pi$ raw invariant mass distribution for a particular p_T bin at $|y| < 0.5$ for minimum bias d+Au collisions (upper panel) and for minimum bias p+p collisions (lower panel). The dashed lines are the linear function that describes the residual background.

residual background indicated by a dashed line. In this case, the normalization factor used to subtract the combinatorial background was changed until the best χ^2/ndf was achieved. Similar to the ρ^0 analysis [3], the uncorrected yield of the Δ^{++} was a free parameter in the fit, and the Δ^{++} distribution was corrected for the detector acceptance and efficiency determined from a detailed simulation of the TPC response using GEANT [33]. The relativistic p-wave Breit-Wigner function multiplied by the phase space is the same as Eq. (2). However, in the case of the Δ^{++}, the mass-dependent width is given by

$$\Gamma = \frac{\Gamma_0 M_0}{M_{p\pi}} \times \frac{k(M_{p\pi})^3 F(\Lambda_\pi, k(M_{p\pi}))^2}{k(M_0)^3 F(\Lambda_\pi, k(M_0))^2}, \tag{5}$$

where $F(\Lambda_\pi, k_{\text{c.m.}})$ is the form factor used to fit the π-N scattering phase shift with $\Lambda_\pi = 290$ MeV/c^2 [42], and

$$k(M_{p\pi})^2 = \frac{\left(M_{p\pi}^2 - m_p^2 - m_\pi^2\right)^2 - 4m_p^2 m_\pi^2}{4M_{p\pi}^2}. \tag{6}$$

The Δ^{++} mass and width at $|y| < 0.5$ for minimum bias d+Au interactions as a function of p_T are depicted in Fig. 13. The Δ^{++} mass is significantly smaller than the values

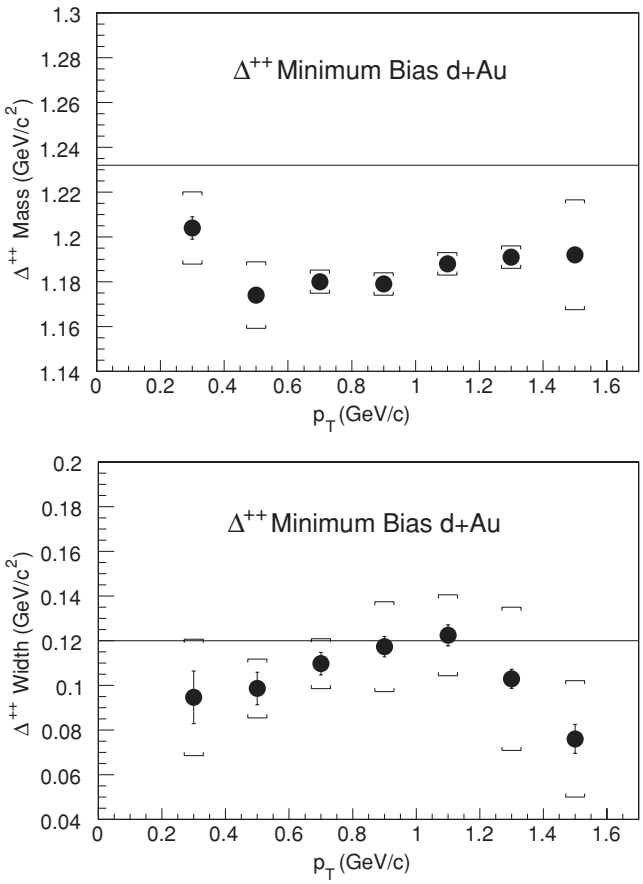

FIG. 13. Δ^{++} mass (upper panel) and width (lower panel) as functions of p_T at $|y| < 0.5$ for minimum bias d+Au collisions. The solid lines are the PDG Δ^{++} mass (1.232 GeV/c^2) and width (0.120 GeV/c^2) [26]. The brackets indicate the systematic uncertainties.

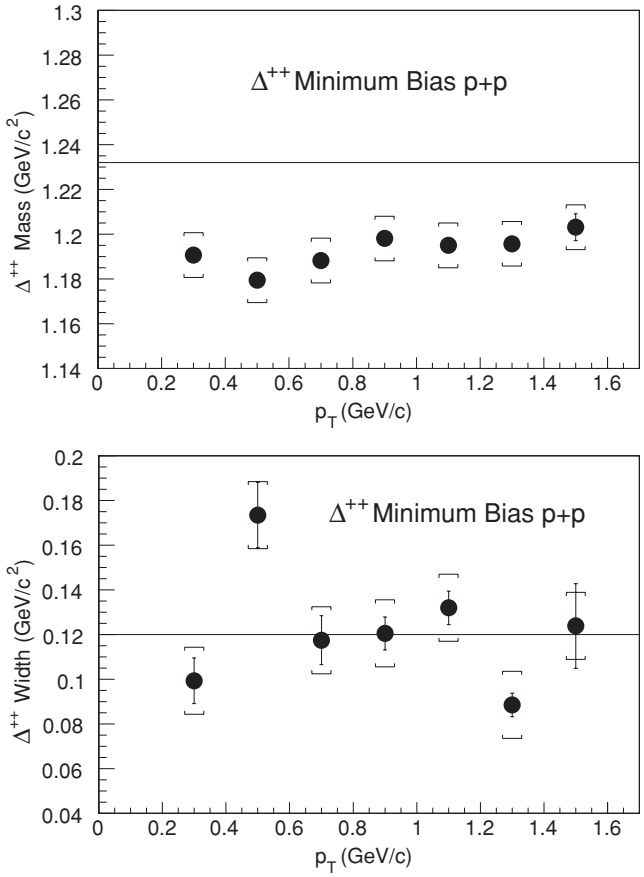

FIG. 14. Δ^{++} mass (upper panel) and width (lower panel) as functions of p_T at midrapidity for minimum bias p+p interactions. The solid lines are the PDG Δ^{++} mass (1.232 GeV/c^2) and width (0.120 GeV/c^2) [26]. The brackets indicate the systematic uncertainties.

previously reported, though the width is in agreement within errors [26]. Possible explanations for a Δ^{++} mass shift are the same as for the ρ^0 [3].

The Δ^{++} mass and width at midrapidity for minimum bias p+p collisions as a function of p_T are shown in Fig. 14. The analysis procedure in minimum bias p+p is the same as in d+Au collisions. Similar to the d+Au measurement, the Δ^{++} mass is significantly smaller than the values in Ref. [26] and the same possible explanations apply. The Δ^{++} width is in agreement with previous values within errors [26].

For the Δ^{++} mass and width, the main contributions to the systematic uncertainties were calculated as a function of p_T by using different residual background functions (first- and second-order polynomial) and different slope parameters in the BW×PS function. The mass and the width were also obtained separately for Δ^{++} and $\bar{\Delta}^{--}$. The contribution due to the uncertainty in the measurement of particle momenta is ∼5 MeV/c^2. The systematic uncertainty can be as large as ∼20 and ∼30 MeV/c^2 for the Δ^{++} mass and width, respectively. In p+p collisions, the systematic uncertainty on the mass and the width was evaluated similarly to the measurement in d+Au collisions. The systematic uncertainty is ∼10 MeV/c^2 and ∼15 MeV/c^2 for the Δ^{++} mass and width, respectively.

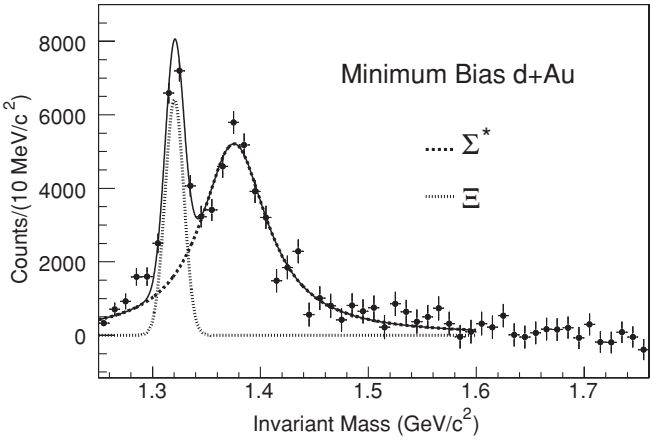

FIG. 15. Mixed-event background subtracted $\Lambda\pi$ raw invariant mass distribution integrated over the Σ^* p_T at $|y| < 0.75$ for minimum bias d+Au collisions.

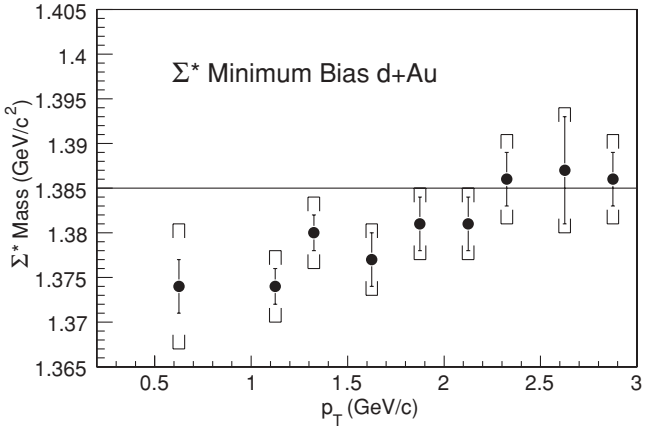

FIG. 17. Σ^* mass as a function of p_T at $|y| < 0.75$ for minimum bias d+Au collisions. The solid line is the PDG Σ^* mass average between the masses of Σ^{*+} and Σ^{*-} (1.3850 GeV/c^2) [26]. The brackets indicate the systematic uncertainties.

The midrapidity and p_T integrated $\Lambda\pi$ (Σ^*) and pK (Λ^*) raw invariant mass distributions, after the mixed-event background subtraction, from minimum bias d+Au collisions are depicted in Figs. 15 and 16, respectively. The signal-to-background ratio is 1/14 for the Σ^* and 1/24 for the Λ^* before mixed-event background subtraction. Since the Ξ^- and the $\bar{\Xi}^+$ have the same final state as the Σ^{*-} and $\bar{\Sigma}^{*+}$, the $\Lambda\pi$ invariant mass distribution is fitted to a Gaussian combined with a nonrelativistic Breit-Wigner function (SBW)

$$\mathrm{SBW} = \frac{\Gamma_0}{(M_{\Lambda\pi} - M_0)^2 + \Gamma^2/4}. \tag{7}$$

In the case of the Λ^*, the signal is fitted to a nonrelativistic Breit-Wigner function combined with a linear function that describes the residual background [7].

The fit parameters corresponding to the Σ^* mass and width in the integrated p_T interval ($0.25 < p_T < 3.5$ GeV/c) are $1.376 \pm 0.002 \pm 0.007$ GeV/c^2 and $48 \pm 2 \pm 10$ MeV/c^2, respectively. Both the measured width and the mass, within their uncertainty, are in agreement with the PDG values of the Σ^* [26]. The systematic errors include the uncertainty due to choice of bin size, the normalization of the mixed-event background, the variations in the fit range, and the selections of event and tracks. It is possible to further study the p_T dependence of the Σ^* mass when the width is fixed to the PDG value (37.6 ± 1.1 MeV/c^2) [26] and the mass is a free parameter in the Breit-Wigner function. Figure 17 shows the p_T dependence for the Σ^* mass from the fit function. There is a small difference in the mass for low p_T Σ^* compared to the PDG value.

The results for the Λ^* mass and width are shown in Figs. 18 and 19, respectively. The Λ^* mass obtained from the data is $1515.0 \pm 1.2 \pm 3$ MeV/c^2, consistent with the Λ^* natural mass of 1519.5 ± 1.0 MeV/c^2 [26] within errors. The width of the p_T integrated spectrum is $40 \pm 5 \pm 10$ MeV/c^2, which includes the intrinsic resolution of the detector [33] of 6 MeV and the momentum-dependent mass shifts in the

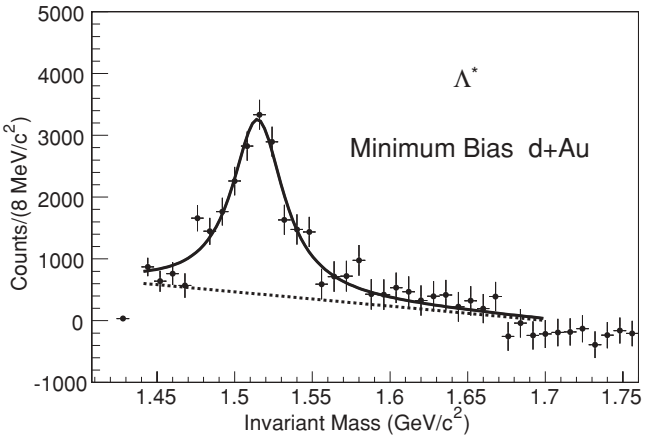

FIG. 16. Mixed-event background subtracted pK raw invariant mass distribution integrated over the Λ^* p_T at $|y| < 0.5$ for minimum bias d+Au collisions. The dashed line is the linear function that describes the residual background.

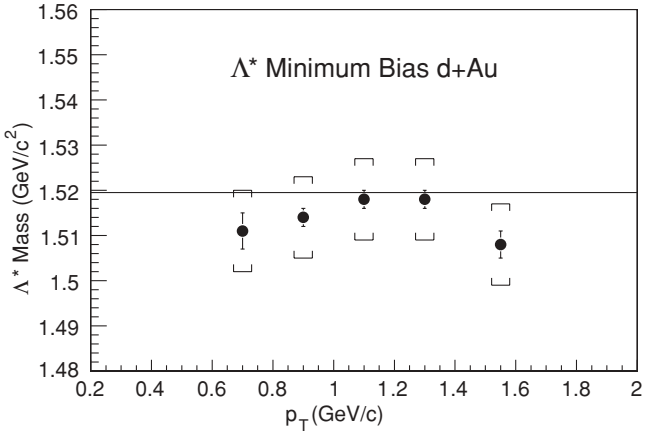

FIG. 18. Λ^* mass as a function of p_T at $|y| < 0.5$ for minimum bias d+Au collisions. The solid line is the PDG Λ^* mass (1.5195 GeV/c^2) [26]. The brackets indicate the systematic uncertainties.

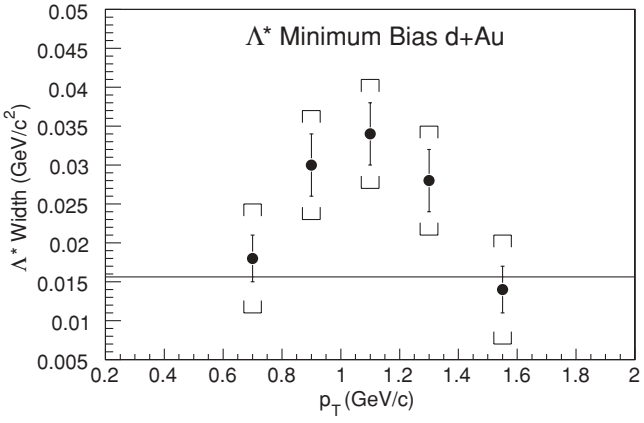

FIG. 19. Λ^* width as a function of p_T at $|y| < 0.5$ for minimum bias d+Au collisions. The solid line is the PDG Λ^* width (0.0156 GeV/c^2) [26]. The brackets indicate the systematic uncertainties. Our simulations, including both the detector resolution and kinetic cuts, show a width of 0.022 GeV/c^2.

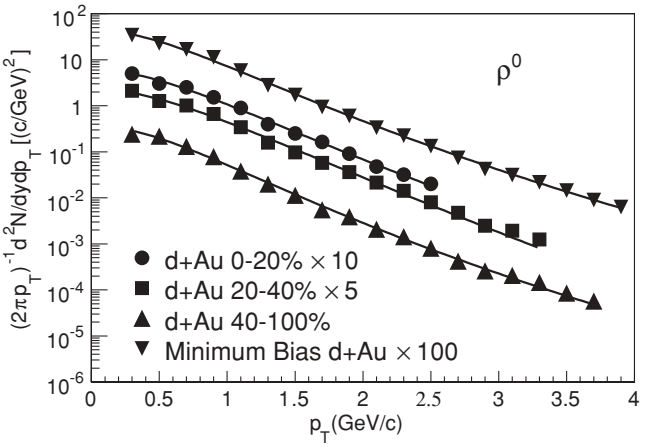

FIG. 20. ρ^0 invariant yields as a function of p_T at $|y| < 0.5$ for minimum bias d+Au interactions and 0–20%, 20–40%, and 40–100% of the total d+Au cross section. The lines are fits to a Levy function [Eq. (8)]. The errors are statistical only and smaller than the symbols.

data, which are in the statistical and systematical limits. The measured width in each momentum bin is consistent with folding the Λ^* natural width of 15.6 ± 1.0 MeV/c^2 [26] with the detector resolution. The systematic uncertainties are due to the residual background, the range used for the normalization and for the fit to the signal, and different bin widths.

In d+Au collisions, we observe modifications of the mass and decay width of short-lived resonances that might be due to dynamical interactions with the surrounding matter, interference, phase space, and Bose-Einstein correlations [3].

B. Spectra

In p+p collisions at RHIC, a shape difference in the p_T spectra of mesons and baryons for nonresonant particles in the interval $2 < p_T < 6$ GeV/c at $\sqrt{s_{NN}} = 200$ GeV was observed [41]. To verify if such effect is observed in d+Au collisions for resonances, their spectra are studied.

The uncorrected yields obtained in each p_T bins were corrected for the detector acceptance and efficiency determined from a detailed simulation of the TPC response using GEANT [33]. The yields were also corrected for the corresponding branching ratios listed in Table I, to account for the fact that we only measure certain decay modes.

The ρ^0 and the $(K^* + \overline{K^*})/2$ corrected invariant yields $[d^2N/(2\pi p_T\, dp_T\, dy)]$ at $|y| < 0.5$ as a function of p_T for minimum bias d+Au interactions are shown in Figs. 20 and 21, respectively. A Levy function [4]

$$\frac{1}{2\pi p_T}\frac{d^2N}{dy\,dp_T} = \frac{dN}{dy}\frac{(n-1)(n-2)}{2\pi nT[nT + m_0(n-2)]} \times \left(1 + \frac{\sqrt{p_T^2 + m_0^2} - m_0}{nT}\right)^{-n} \quad (8)$$

was used to extract the ρ^0 and K^* yields per unit of rapidity around midrapidity. In the limit of low p_T, the Levy function is an exponential function and a power law in the limit of high p_T.

The $(\Delta^{++} + \bar{\Delta}^{--})/2$, $(\Sigma^{*-} + \bar{\Sigma}^{*+})/2$, and $(\Lambda^* + \bar{\Lambda}^*)/2$ corrected invariant yields at $|y| < 0.5$ as a function of p_T are shown in Figs. 22, 23, and 24, respectively. Figure 22 also depicts the $(\Delta^{++} + \bar{\Delta}^{--})/2$ corrected invariant yield for minimum bias p+p. Since the p_T region is limited to low p_T, we use an exponential function [4]

$$\frac{1}{2\pi m_T}\frac{d^2N}{dy\,dm_T} = \frac{dN}{dy}\frac{1}{2\pi T(m_0 + T)}\exp\left(\frac{-(m_T - m_0)}{T}\right), \quad (9)$$

to extract the Δ^{++}, Σ^*, and Λ^* yields per unit of rapidity around midrapidity. Due to limited statistics, only the Λ^* yield in minimum bias d+Au collisions was measured.

The extracted dN/dy, T, and n for the ρ^0 and the K^* are listed in Table V. In the case of the Δ^{++}, Σ^*, and Λ^*,

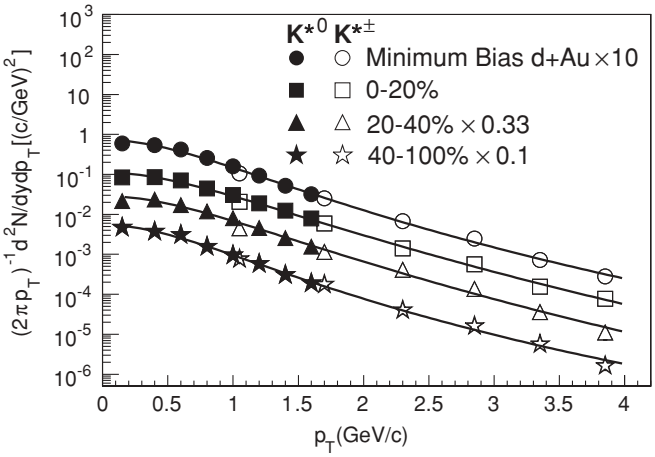

FIG. 21. $(K^* + \bar{K}^*)/2$ together with the $(K^{*+} + K^{*-})/2$ invariant yields as a function of p_T at $|y| < 0.5$ for minimum bias d+Au collisions and three different centralities. The lines are fits to a Levy function [Eq. (8)]. The errors are statistical only and smaller than the symbols.

TABLE V. ρ^0 and $(K^* + \bar{K}^*)/2$ dN/dy, T, and n at $|y| < 0.5$ measured in minimum bias d+Au collisions and 0–20%, 20–40%, and 40–100% of the total d+Au cross section. The first error is statistical; the second is systematic.

Resonance	Centrality	dN/dy	T (MeV)	n
ρ^0	Minimum bias d+Au	$0.812 \pm 0.004 \pm 0.085$	$231.7 \pm 1.6 \pm 35$	11.1 ± 0.2
	0–20%	$1.169 \pm 0.014 \pm 0.17$	$245 \pm 6 \pm 52$	13.6 ± 1.7
	20–40%	$0.958 \pm 0.011 \pm 0.14$	$230 \pm 4 \pm 44$	11.4 ± 0.6
	40–100%	$0.607 \pm 0.005 \pm 0.13$	$212 \pm 3 \pm 36$	10.7 ± 0.4
K^*	Minimum bias d+Au	$0.161 \pm 0.002 \pm 0.027$	$286 \pm 7 \pm 44$	10.4 ± 0.1
	0–20%	$0.294 \pm 0.009 \pm 0.051$	$316 \pm 22 \pm 53$	12.8 ± 0.4
	20–40%	$0.204 \pm 0.005 \pm 0.037$	$306 \pm 17 \pm 50$	12.5 ± 0.3
	40–100%	$0.108 \pm 0.002 \pm 0.018$	$232 \pm 7 \pm 39$	7.3 ± 0.6

the corresponding dN/dy and T are listed in Table VI. One contribution to the systematic uncertainties quoted in Tables V and VI is due to the tracking efficiency (∼8%), which is common to all measurements.

In the case of the ρ^0, the normalization between the $M_{\pi\pi}$ and the like-sign reference distributions is the largest contribution to the systematic uncertainty to the yield and the inverse slope (T), and it can be as large as ∼20%. If the ρ^0 invariant yield is obtained for the case that the ρ^0 width is a free parameter in the hadronic cocktail, the invariant yield increases by 22% from those shown in Table V. In the other extreme, if the invariant yield is obtained by assuming an exponential background, the yields decrease by 45%.

The contributions to the systematic uncertainty on the K^* and Δ^{++} yields and T measured in d+Au collisions were obtained by comparing different BW functions (relativistic and nonrelativistic), using different residual background functions (first- and second-order polynomial), different functions to fit the spectra (exponential and power-law), and different slope parameters in the BW×PS function (140 MeV and 180 MeV). In addition, the yields and T were obtained separately for K^{*0}, $\bar{K}^{*0}$, K^{*+}, K^{*-}, Δ^{++}, and $\bar{\Delta}^{--}$. The effect of opening the primary vertex from 50 to 75 cm in the case of the yields obtained for different centralities in d+Au collisions was also taken into account. The systematic uncertainty on both yields and T is ∼20% for the K^*. For the Δ^{++}, the systematic uncertainties are 12% and 17%, respectively.

In minimum bias p+p collisions, the main contributions to the Δ^{++} yield and T systematic uncertainty were estimated from the invariant yields as a function of p_T by increasing the normalization between the $M_{p\pi}$ and the mixed-event reference distributions until the fit to the Δ^{++} signal was not reasonable. This procedure was then repeated by decreasing the normalization. During this procedure, the width was fixed to 110 MeV/c^2 [42].

The number of partons (primarily gluons) in a nucleus grows very rapidly at very high energies. If the occupation number of these partons is large, they may saturate and form a novel state of matter called a color glass condensate (CGC). This CGC has a bulk scale that is the typical intrinsic transverse momentum of the saturated gluons in the nucleus. The CGC can be probed in deep inelastic scattering [43,44], in photoproduction in peripheral heavy-ion collisions [45], in $p(d)$+A collisions [46,47], and in heavy-ion collisions [48–50]. Figure 25 shows that the transverse mass m_T spectra of identified hadrons follow a generalized scaling

TABLE VI. $(\Delta^{++} + \bar{\Delta}^{--})/2$, $(\Sigma^* + \bar{\Sigma}^*)/2$, and $(\Lambda^* + \bar{\Lambda}^*)/2$ dN/dy and T at $|y| < 0.5$ measured in minimum bias d+Au collisions and 0–20%, 20–40%, and 40–100% of the total d+Au cross section. For Δ^{++}, the results from the measurements in minimum bias p+p are also shown. The first error is statistical; the second is systematic.

Resonance	Centrality	dN/dy	T (MeV)
Δ^{++}	Minimum bias d+Au	$0.0823 \pm 0.0012 \pm 0.0099$	$284 \pm 7 \pm 45$
	0–20%	$0.177 \pm 0.005 \pm 0.021$	$328 \pm 17 \pm 52$
	20–40%	$0.116 \pm 0.003 \pm 0.014$	$303 \pm 14 \pm 48$
	40–100%	$0.0529 \pm 0.0008 \pm 0.0063$	$290 \pm 9 \pm 46$
	Minimum bias p+p	$0.0139 \pm 0.0008 \pm 0.0050$	$216 \pm 13 \pm 86$
Σ^*	Minimum bias d+Au	$0.0319 \pm 0.0011 \pm 0.0041$	$387 \pm 11 \pm 28$
	0–20%	$0.068 \pm 0.006 \pm 0.011$	$473 \pm 39 \pm 40$
	20–40%	$0.040 \pm 0.004 \pm 0.007$	$420 \pm 36 \pm 40$
	40–100%	$0.018 \pm 0.002 \pm 0.005$	$428 \pm 36 \pm 40$
Λ^*	Minimum bias d+Au	$0.0149 \pm 0.0014 \pm 0.0022$	$392 \pm 75 \pm 39$

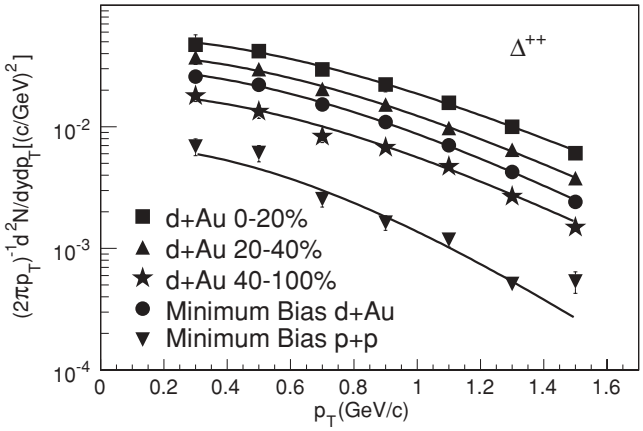

FIG. 22. $(\Delta^{++} + \bar{\Delta}^{--})/2$ invariant yields as a function of p_T at $|y| < 0.5$ for minimum bias p+p, d+ Au interactions, and 0–20%, 20–40%, and 40–100% of the total d+Au cross section. The lines are fits to an exponential function [Eq. (9)]. The errors are statistical only and smaller than the symbols for the spectra measured in d+Au. In the p+p measurement, the errors shown also include the systematic uncertainties.

law in d+Au collisions between $1 \leqslant m_T \leqslant 2$ GeV/c^2. Even though this scaling behavior is motivated by the idea of a saturation of the gluon density, the identified particle spectra measured in p+p collisions at energies available at the CERN Intersecting Storage Rings (ISR) [51–53], CERN Super Proton Synchrotron (SPS) accelerator [54], and RHIC [41] have also been shown to follow a generalized scaling law in transverse mass. More theoretical work is needed to explain the similarities between p+p and d+Au collisions.

It is interesting to notice that for resonances in d+Au collisions in the p_T region measured, we do not observe the shape difference of the p_T spectra observed for mesons and baryons in p+p collisions at RHIC [41] for nonresonant particles in the interval $2 < p_T < 6$ GeV/c at the same beam energy. This baryon-meson effect observed in p+p collisions was argued to be a simple reflection of the underlying dynamics of the collision in that meson production from

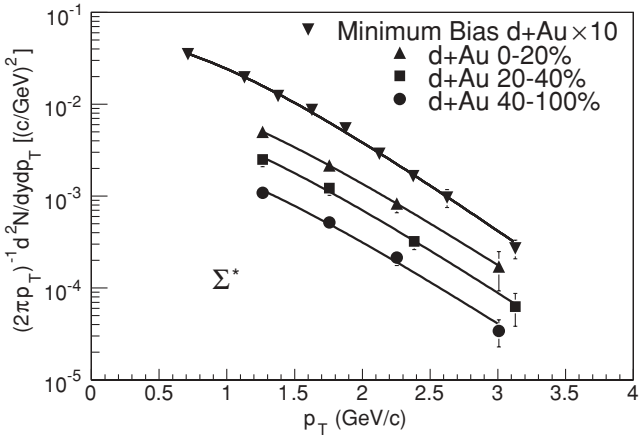

FIG. 23. Σ^* invariant yields as a function of p_T at $|y| < 0.75$ for minimum bias d+Au collisions and three different centralities. The lines are fits to an exponential function [Eq. (9)].

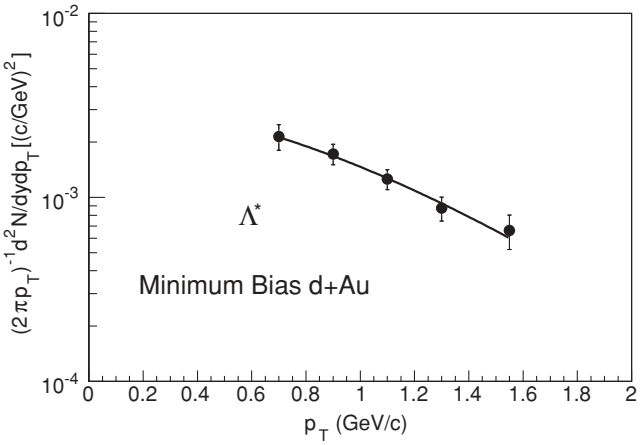

FIG. 24. Λ^* invariant yields as a function of p_T at $|y| < 0.5$ for minimum bias d+Au collisions. The line is a fit to an exponential function [Eq. (9)].

fragmentation requires only a (quark, antiquark) pair, while baryon production requires a (diquark, antidiquark) pair.

C. Mean transverse momenta $\langle p_T \rangle$

The averaged transverse momentum $\langle p_T \rangle$ provides information on the shape of the particle spectra. At a given mass, the larger the $\langle p_T \rangle$, the harder the spectra. The resonance $\langle p_T \rangle$ were calculated from the fit parameters depicted in Tables V and VI and are listed in Table VII.

The ρ^0, K^*, Δ^{++}, Λ^*, and Σ^* $\langle p_T \rangle$ as functions of $dN_{\rm ch}/d\eta$ compared with those of π^-, K^-, and $\bar{p}$ for minimum bias d+Au [55] are depicted in Figs. 26 and 27. While the $\langle p_T \rangle$ of these hadrons are independent of centrality as expected, the $\langle p_T \rangle$ is strongly dependent on the mass of the particle.

We can compare the spectra shape among particles for different systems by comparing their $\langle p_T \rangle$. Figure 28 shows the $\langle p_T \rangle$ of various particles for different systems, minimum bias

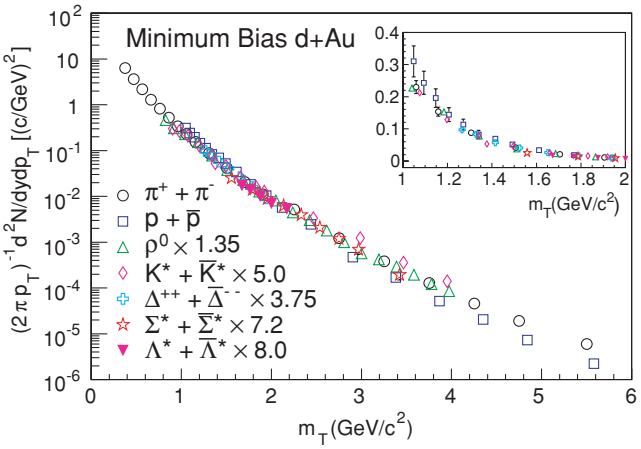

FIG. 25. (Color online) Proton and pion spectra [56] plotted together with the rescaled minimum bias d+Au spectra of ρ^0, K^*, Δ^{++}, and Σ^*, where the transverse mass scaling is observed. The inset plot is a zoom-in of the region $1 \leqslant m_T \leqslant 2$ GeV/c^2 on a linear scale.

TABLE VII. The ρ^0, K^*, Δ^{++}, Σ^*, and Λ^* $\langle p_T \rangle$ in minimum bias d+Au collisions and 0–20%, 20–40%, and 40–100% of the total d+Au cross section. The $\langle p_T \rangle$ measured in minimum bias p+p are also listed. The first error is statistical; the second is systematic.

Resonance	Centrality	$\langle p_T \rangle$ (GeV/c)
ρ^0	Minimum bias d+Au	$0.808 \pm 0.050 \pm 0.086$
	0–20%	$0.815 \pm 0.020 \pm 0.083$
	20–40%	$0.805 \pm 0.015 \pm 0.082$
	40–100%	$0.764 \pm 0.009 \pm 0.081$
	Minimum bias p+p	$0.616 \pm 0.002 \pm 0.062$
K^*	Minimum bias d+Au	$0.96 \pm 0.02 \pm 0.16$
	0–20%	$1.00 \pm 0.07 \pm 0.17$
	20–40%	$0.98 \pm 0.05 \pm 0.17$
	40–100%	$0.90 \pm 0.03 \pm 0.15$
	Minimum bias p+p	$0.81 \pm 0.02 \pm 0.14$
Δ^{++}	Minimum bias d+Au	$0.89 \pm 0.02 \pm 0.14$
	0–20%	$0.98 \pm 0.05 \pm 0.16$
	20–40%	$0.92 \pm 0.04 \pm 0.18$
	40–100%	$0.90 \pm 0.03 \pm 0.14$
	Minimum bias p+p	$0.63 \pm 0.04 \pm 0.13$
Σ^*	Minimum bias d+Au	$1.13 \pm 0.03 \pm 0.08$
	0–20%	$1.33 \pm 0.06 \pm 0.10$
	20–40%	$1.20 \pm 0.07 \pm 0.10$
	40–100%	$1.22 \pm 0.07 \pm 0.10$
	Minimum bias p+p	$1.015 \pm 0.015 \pm 0.07$
Λ^*	Minimum bias d+Au	$1.17 \pm 0.15 \pm 0.12$
	Minimum bias p+p	$1.08 \pm 0.09 \pm 0.05$

p+p and d+Au, and central Au+Au collisions. Even though there is a strong mass dependence, the $\langle p_T \rangle$ of these particles do not appear to strongly depend on the collision system, with the exception of the $\bar{p}$. However, the $\langle p_T \rangle$ of particles measured in d+Au collisions lie between the $\langle p_T \rangle$ measured in p+p and Au+Au collisions, indicating a hardening of the spectra from p+p through d+Au to Au+Au collisions.

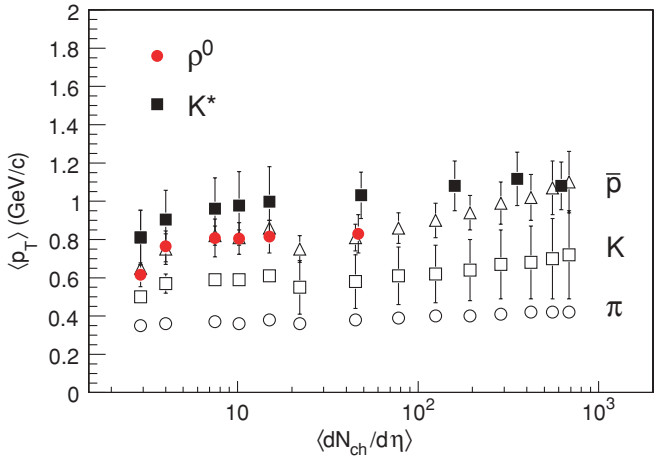

FIG. 26. (Color online) ρ^0 and K^* $\langle p_T \rangle$ as a function of $\langle dN_{\rm ch}/d\eta \rangle$ compared with that of π^-, K^-, and $\bar{p}$ for minimum bias p+p, minimum bias d+Au, and 0–20%, 20–40%, and 40–100% of the total d+Au cross section [55]. The errors shown are the quadratic sum of the statistical and systematic uncertainties.

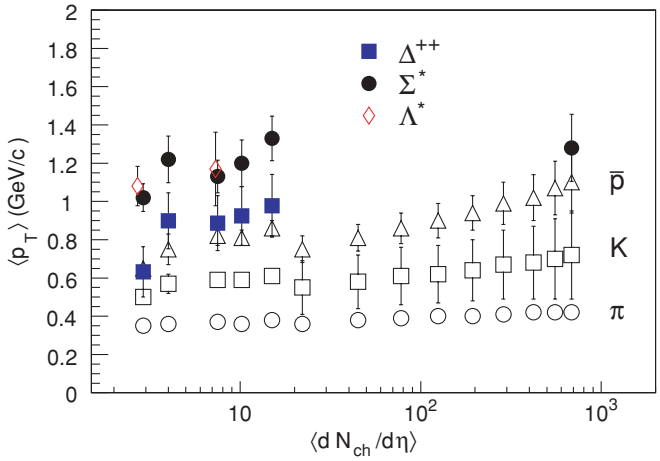

FIG. 27. (Color online) Δ^{++}, Σ^*, and Λ^* $\langle p_T \rangle$ as a function of $\langle dN_{\rm ch}/d\eta \rangle$ compared with those of π^-, K^-, and $\bar{p}$ for minimum bias p+p, minimum bias d+Au, and 0–20%, 20–40%, and 40–100% of the total d+Au cross section [55]. The errors shown are the quadratic sum of the statistical and systematic uncertainties.

The main contributions to the systematic uncertainties quoted in Table VII are due to tracking efficiency (∼8%) and different fit functions used to fit the p_T spectra. In the case of the ρ^0, there was in addition the normalization between the $\pi^+\pi^-$ invariant mass distribution and the like-sign reference distributions (∼5%).

D. Particle ratios

It has been previously shown that the ratio of yields of resonances to the yields of stable particles can effectively probe the dynamics of relativistic heavy-ion collisions [2–4,7]. The ratios of yields of resonances to stable particles with similar quark contents but different spins and masses are given in Table VIII. The values of π, K, and p were taken from [56,57]. Figures 29–33 show the ratios of resonances to their corresponding stable particles as functions of the charged particle

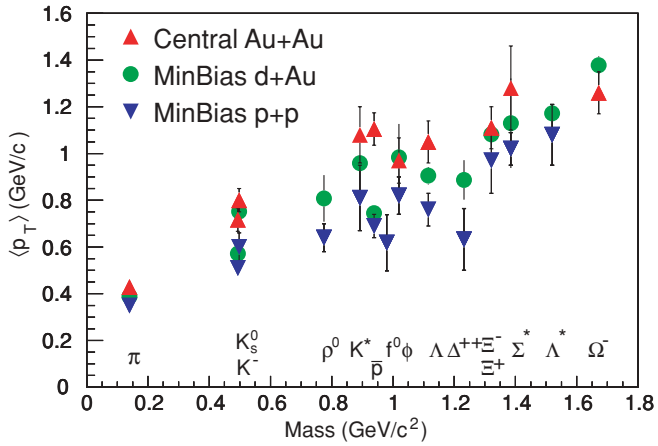

FIG. 28. (Color online) $\langle p_T \rangle$ of various particles for different systems, minimum bias p+p and d+Au, and central Au+Au collisions. The errors shown are the quadratic sum of the statistical and systematic uncertainties.

TABLE VIII. ρ^0/π^-, K^*/K^-, Δ^{++}/p, Σ^*/Λ, and Λ^*/Λ ratios in minimum bias p+p [3,4,7], d+Au, and 0–20%, 20–40%, and 40–100% of the total d+Au cross section. The first error is statistical; the second is systematic.

Centrality	ρ^0/π^-	K^*/K^-	Δ^{++}/p	Σ^*/Λ	Λ^*/Λ
Min. bias d+Au	$0.175 \pm 0.004 \pm 0.054$	$0.28 \pm 0.01 \pm 0.03$	$0.185 \pm 0.005 \pm 0.028$	0.23 ± 0.03	0.106 ± 0.024
0–20%	$0.139 \pm 0.014 \pm 0.036$	$0.29 \pm 0.01 \pm 0.03$	$0.206 \pm 0.006 \pm 0.028$	0.24 ± 0.04	
20–40%	$0.158 \pm 0.011 \pm 0.056$	$0.29 \pm 0.01 \pm 0.03$	$0.192 \pm 0.005 \pm 0.028$	0.21 ± 0.04	
40–100%	$0.211 \pm 0.005 \pm 0.068$	$0.34 \pm 0.01 \pm 0.04$	$0.203 \pm 0.006 \pm 0.028$	0.23 ± 0.06	
Min. bias p+p	$0.183 \pm 0.001 \pm 0.027$	$0.35 \pm 0.01 \pm 0.05$	$0.132 \pm 0.002 \pm 0.049$	0.029 ± 0.047	0.092 ± 0.026

multiplicity ($N_{\rm ch}$) in p+p, d+Au, and Au+Au collisions. We observe that the ρ^0/π^-, Δ^{++}/p, and Σ^*/Λ ratios are independent of multiplicity, while the K^*/K^- and Λ^*/Λ ratios seem to decrease. The resonance abundance could be affected by mass shifts due to phase space [$\exp(-m/T)$] in different collision systems.

The resonance ratios normalized by their value measured in p+p collisions at the same $\sqrt{s}$ are plotted in Fig. 34. The decrease of the resonance ratios of K^*/K^- and Λ^*/Λ from p+p to Au+Au collisions has been explained by an extended lifetime of the hadronic phase where the rescattering of the decay particles dominates over resonance regeneration [2,4,7–9,13]. As the K^*/K^- and the Λ^*/Λ ratios are similar for p+p and d+Au collisions, this would suggest the absence of an extended hadronic medium in d+Au collisions. The ρ^0/π^-, Δ^{++}/p, and Σ^*/Λ ratios in d+Au collisions are in agreement with their ratios measured in p+p collisions. These resonance ratios do not show any suppression from p+p to Au+Au collisions either, hence they are not sensitive to the lifetime of the hadronic medium, presumably because of their large regeneration cross section.

The ρ^0/π^- ratio is independent of centrality up to the 40–80% of the inelastic hadronic Au+Au cross section, and it is of the same order as the corresponding p+p measurement. In p+p collisions, it has been proposed that the mass shift is due to $\pi\pi$ rescattering, even in the absence of a medium [35]. If this is the case, $\pi^+\pi^-$ rescattering might regenerate the ρ^0. In addition, one of the decay daughters might also rescatter with other hadrons preventing the ρ^0 to be measured. Therefore, these two processes compete with (and balance) each other.

E. Nuclear modification factor

The nuclear modification factor $R_{d\rm Au}$ is defined as

$$R_{d\rm Au}(p_T) = \frac{d^2N_{d\rm Au}/dy\,dp_T}{\left(\langle N_{\rm bin}\rangle/\sigma_{pp}^{\rm inel}\right)\left(d^2\sigma_{pp}/dy\,dp_T\right)}, \qquad (10)$$

where $d^2N_{d\rm Au}/dy\,dp_T$ is the yield of the produced particles in minimum bias d+Au collisions, $d^2\sigma_{pp}/dy\,dp_T$ is the inclusive cross section in p+p collisions, $\langle N_{\rm bin}\rangle$ is the average number of binary nucleon-nucleon (NN) collisions per event, and $\langle N_{\rm bin}\rangle/\sigma_{pp}^{\rm inel}$ is the nuclear overlap $T_A(b)$ [23,58,59]. The value of $\sigma_{pp}^{\rm inel}$ is 42 mb.

The enhancement observed in $R_{d\rm Au}$ for high p_T and midrapidity, known as the Cronin effect [19], is generally attributed to the influence of multiple parton scattering through matter prior to the hard scattering that produces the observed high-p_T hadron [60]. Therefore, the nuclear modification

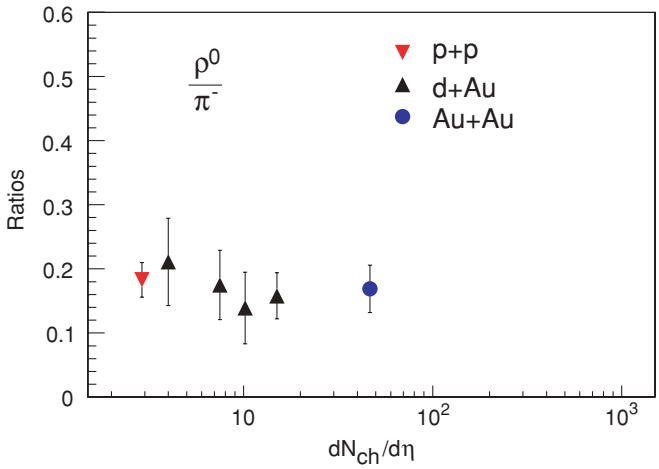

FIG. 29. (Color online) ρ^0/π^- ratios in p+p, various centralities in d+Au, and in peripheral Au+Au collisions as a function of $dN_{\rm ch}/d\eta$. The errors shown are the quadratic sum of the statistical and systematic uncertainties.

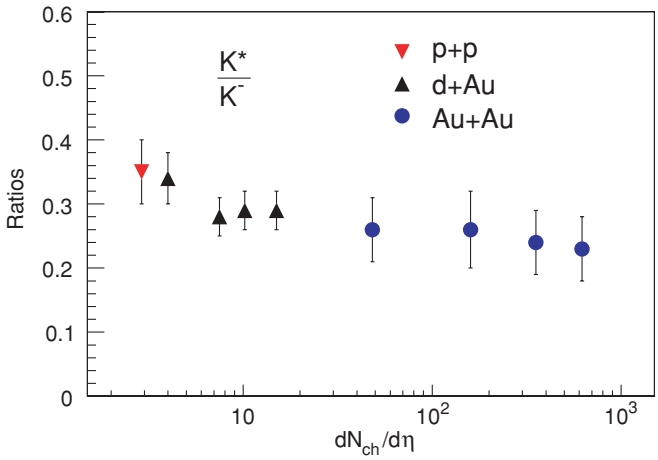

FIG. 30. (Color online) K^*/K^- ratios in p+p and various centralities in d+Au and Au+Au collisions as a function of $dN_{\rm ch}/d\eta$. The errors shown are the quadratic sum of the statistical and systematic uncertainties.

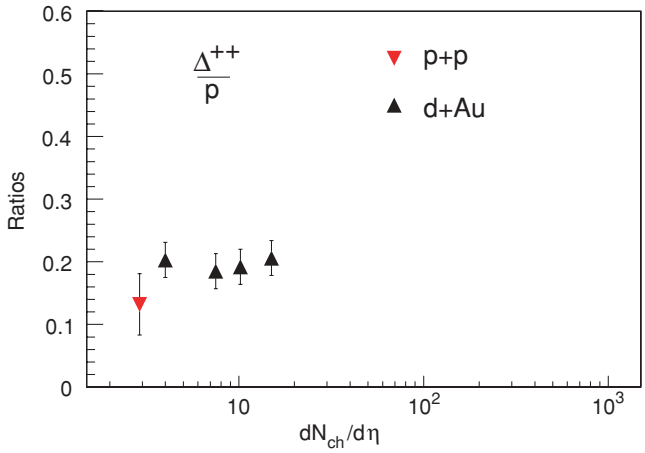

FIG. 31. (Color online) Δ^{++}/p ratios in $p+p$ and various centralities in $d+$Au collisions as a function of $dN_{\rm ch}/d\eta$. The errors shown are the quadratic sum of the statistical and systematic uncertainties.

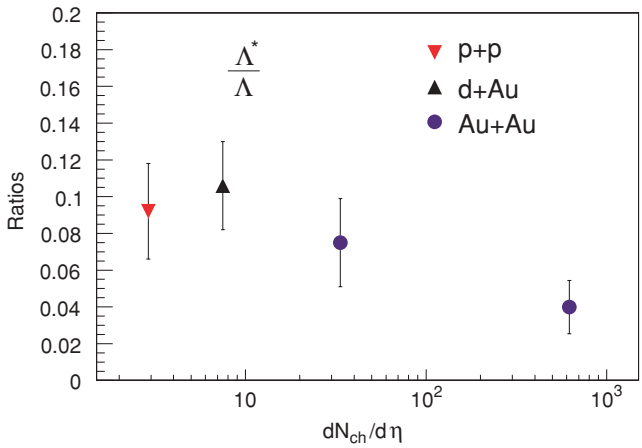

FIG. 33. (Color online) Λ^*/Λ ratios in $p+p$, minimum bias $d+$Au, and two different centralities in Au+Au collisions as a function of $dN_{\rm ch}/d\eta$. The errors shown are the quadratic sum of the statistical and systematic uncertainties.

factor $R_{d\rm Au}$ can be used to study the effects of matter on particle production.

The $R_{d\rm Au}$ for ρ^0, K^*, and Σ^* are shown in Figs. 35–37 together with the $R_{d\rm Au}$ of charged hadrons and charged pions. The K^* and Σ^* $R_{d\rm Au}$ are lower than unity at low p_T and consistent with the $R_{d\rm Au}$ of charged hadrons and charged pions. The $R_{d\rm Au}$ of the ρ^0, K^*, and Σ^* scale with $N_{\rm bin}$ for $p_T > 1.2$ GeV/c taking into account the uncertainties in the normalization. We also observe that the ρ^0 $R_{d\rm Au}$ for $p_T > 1.5$ GeV/c is suppressed compared to the charged hadrons and charged pions $R_{d\rm Au}$. The Δ^{++} $R_{d\rm Au}$ is not shown because of the small p_T range covered and the large uncertainties in the measurement.

More information may be obtained from the $R_{d\rm Au}$ measurement if it is extended to higher p_T. In the STAR experiment, this will be possible with the installation of the barrel time-of-flight (TOF) detector. The TOF will provide essential particle identification by, for instance, increasing the percentage of kaon and protons for which particle identification is possible to more than 95% of all those produced within the acceptance of the TOF barrel ($|\eta| \leqslant 1.0$). The improvement in particle identification will allow a decrease in the signal-to-background ratios for the resonance measurements.

V. SUMMARY

Measurements of $\rho(770)^0$, $K^*(892)$, $\Delta(1232)^{++}$, $\Sigma(1385)$, and $\Lambda(1520)$ in $\sqrt{s_{NN}} = 200$ GeV $d+$Au collisions reconstructed via their hadronic decay channels using the STAR detector are presented.

The masses of the ρ^0, K^*, Δ^{++}, $\Sigma(1385)$, and $\Lambda(1520)$ were measured for minimum bias and three different centralities in $d+$Au collisions at $\sqrt{s_{NN}} = 200$ GeV. We observe a ρ^0 mass shift of $\sim$50 MeV/c^2 at low p_T. In addition, the ρ^0 mass measured in 0–20% of the total $d+$Au cross

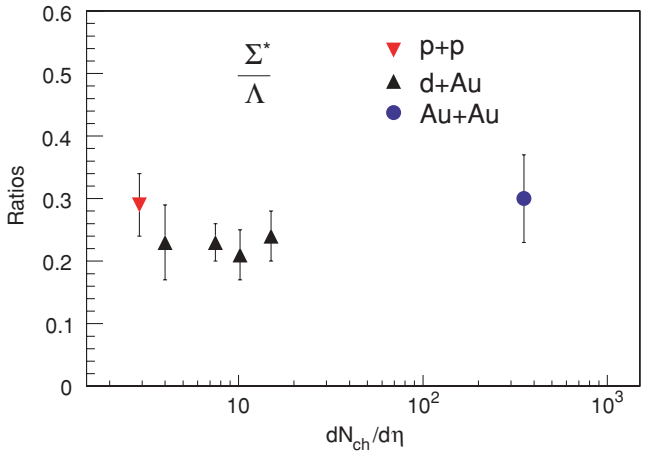

FIG. 32. (Color online) Σ^*/Λ ratios in $p+p$, various centralities in $d+$Au, and in central Au+Au collisions as a function of $dN_{\rm ch}/d\eta$. The errors shown are the quadratic sum of the statistical and systematic uncertainties.

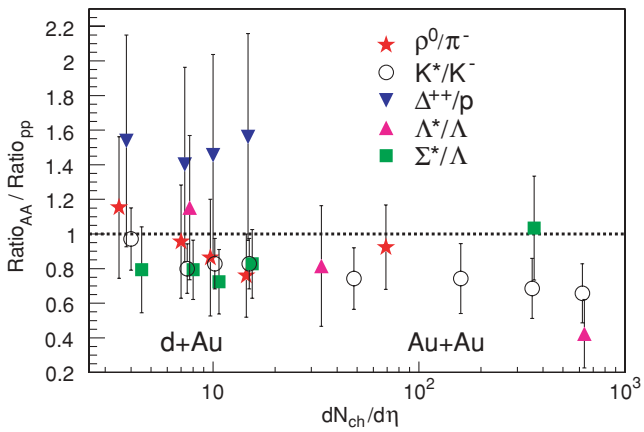

FIG. 34. (Color online) Resonance ratios normalized by their ratio measured in $p+p$ collisions at the same beam energy as a function of $dN_{\rm ch}/d\eta$. The errors shown are the quadratic sum of the statistical and systematic uncertainties.

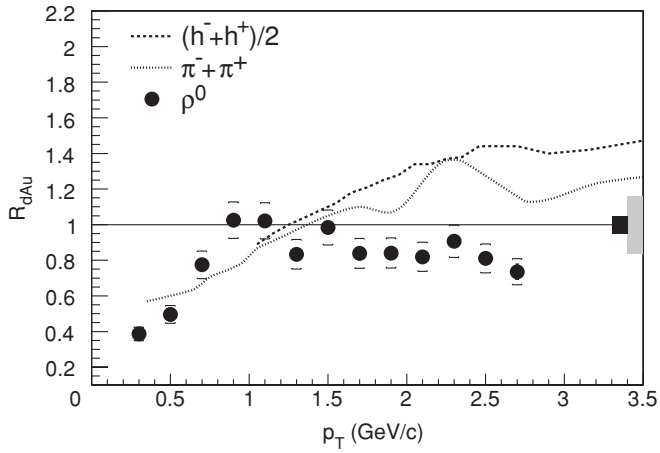

FIG. 35. ρ^0 $R_{d\mathrm{Au}}$ compared with the charged hadrons $R_{d\mathrm{Au}}$. The shaded box is the error on the overall normalization and the black box is the error on N_{bin}.

section is slightly lower than the mass measured in the most peripheral centrality class. We also observe that the ρ^0 mass measured in minimum bias d+Au and high multiplicity p+p interactions are comparable. The K^{*0} and Σ^* masses at low $p_T(p_T < 1.1$ GeV/$c)$ are smaller than previously measured values [26] by up to $\sim$10 MeV/c^2. A similar mass shift for the K^{*0} is observed in minimum bias p+p collisions at $\sqrt{s_{NN}} = 200$ GeV [4]. The $K^{*\pm}$ mass and the K^* width are in agreement with previously reported values within errors [26]. The Δ^{++} mass is shifted by $\sim$40 MeV/c^2 in minimum bias p+p and $\sim$50 MeV/c^2 in minimum bias d+Au collisions. In contrast to the ρ^0, no p_T dependence is observed. Similar mass and/or width modifications with respect to those observed in e+e^- collisions are observed for these resonances in p+p and Au+Au collisions. The possible explanations for the apparent modification of the ρ^0 meson properties are interference between various $\pi^+\pi^-$ scattering channels, phase-space distortions due to the rescattering of pions forming ρ^0, and Bose-Einstein correlations between ρ^0 decay daughters and pions in the surrounding matter [3].

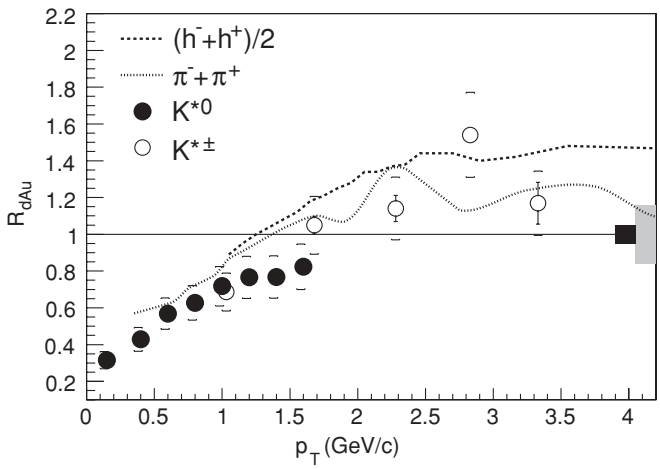

FIG. 36. Same as Fig. 35, but for the K^* $R_{d\mathrm{Au}}$.

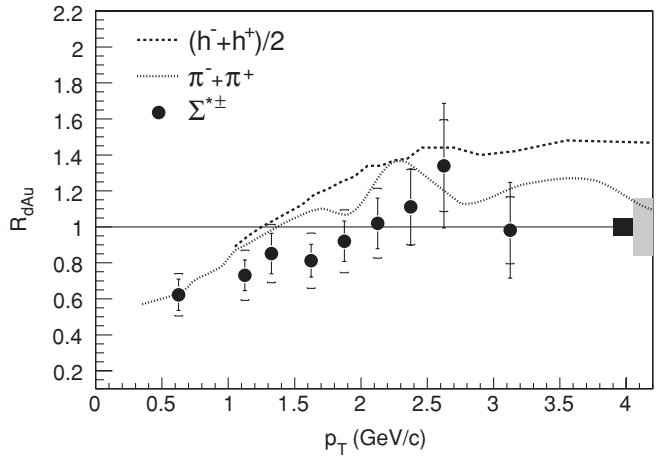

FIG. 37. Same as Fig. 35, but for Σ^* $R_{d\mathrm{Au}}$.

All these explanations require an interaction, which implies a medium such as the one formed in A+A collisions. However, the ρ^0 mass shift measured in p+p collisions [3] can be described without a medium [35]. The Δ^{++} width and the Λ^* mass and width measured are in agreement with previous measurements [26].

The transverse mass spectra follows a generalized scaling law between 1 and 2 GeV/c^2. However, in Au+Au collisions at RHIC at $\sqrt{s_{NN}} = 200$ and 62.4 GeV, a generalized scaling law is not observed [61], possibly because of additional physics effects such as flow, coalescence, and energy loss. Even though the scaling behavior in d+Au collisions is motivated by the idea of a saturation of the gluon density, the identified particle spectra measured in p+p have also been shown to follow a generalized scaling law in transverse mass. More theoretical work is needed to explain the similarities between p+p and d+Au collisions. The resonances in d+Au collisions in the measured p_T region do not show the shape difference of the p_T spectra observed for mesons and baryons in p+p collisions at RHIC for nonresonant particles in the interval $2 < p_T < 6$ GeV/c at the same beam energy. This baryon-meson effect observed in p+p collisions was argued to be a simple reflection of the underlying dynamics of the collision. To have further insight in this matter, the spectra of resonances should be increased to higher momentum, which will be accomplished in STAR with the installation of the barrel time-of-flight detector, which will provide extended particle identification.

The ρ^0, K^*, Δ^{++}, Σ^*, and Λ^* $\langle p_T \rangle$ are found to be centrality independent. Compared with the $\langle p_T \rangle$ of pions, kaons, and antiprotons, the $\langle p_T \rangle$ we measured of these resonances are approximately the same as or even higher than the proton $\langle p_T \rangle$. The resonance $\langle p_T \rangle$ as a function of centrality follow a mass ordering.

The ρ^0/π^-, K^*/K^-, Δ^{++}/p, Σ^*/Λ, and Λ^*/Λ ratios were measured, and we found that the ρ^0/π^- ratio is independent of centrality up to the 40–80% of the inelastic hadronic Au+Au cross section, and it is of the same order of the corresponding p+p measurement. If we speculate that there is particle rescattering even without the presence of a medium for short-lived resonances, then we can interpret these

results in terms of the rescattering/regeneration scenario and conclude that in both cases the regeneration is the dominant process. We observe that the K^*/K^- ratio is the same for $p+p$ and the most peripheral centrality class in $d+$Au collisions. Then, it slightly decreases to peripheral Au+Au collisions to a suppression in central Au+Au collisions, showing that the rescattering is the dominant process. The Σ^*/Λ and the Λ^*/Λ ratios measured in $d+$Au collisions are the same as those measured in $p+p$ collisions within errors, as expected, since they are not as short-lived as the ρ^0, K^*, or Δ^{++}.

The $R_{d\mathrm{Au}}$ of the ρ^0, K^*, and Σ^* scale with N_{bin} for $p_T > 1.2$ GeV/c taking into account the uncertainties in the normalization. We also observed that the ρ^0 $R_{d\mathrm{Au}}$ for $p_T > 1.5$ GeV/c is suppressed compared to the charged hadrons and charged pions $R_{d\mathrm{Au}}$. More information may be obtained from the $R_{d\mathrm{Au}}$ measurement if it is extended to higher p_T, which will be accomplished in the STAR experiment with the installation of the TOF detector.

The measurement of these resonances in $d+$Au collisions will provide a reference for future measurements in $A+A$ collisions.

ACKNOWLEDGMENTS

We thank the RHIC Operations Group and RCF at BNL, and the NERSC Center at LBNL for their support. This work was supported in part by the HENP Divisions of the Office of Science of the U.S. DOE; the U.S. NSF; the BMBF of Germany; IN2P3, RA, RPL, and EMN of France; EPSRC of the United Kingdom; FAPESP of Brazil; the Russian Ministry of Science and Technology; the Ministry of Education and the NNSFC of China; IRP and GA of the Czech Republic; FOM of the Netherlands; DAE, DST, and CSIR of the Government of India; Swiss NSF; the Polish State Committee for Scientific Research; STAA of Slovakia; and the Korea Science & Engineering Foundation.

[1] M. Cheng *et al.*, Phys. Rev. D **74**, 054507 (2006); C. Bernard *et al.*, *ibid.* **75**, 094505 (2007); F. Karsch, hep-ph/0701210.
[2] C. Adler *et al.*, Phys. Rev. C **66**, 061901(R) (2002).
[3] J. Adams *et al.*, Phys. Rev. Lett. **92**, 092301 (2004).
[4] J. Adams *et al.*, Phys. Rev. C **71**, 064902 (2005).
[5] S. Salur, J. Phys. G **32**, S469 (2006).
[6] S. Salur, Ph.D. thesis, Yale University, 2006.
[7] B. I. Abelev *et al.*, Phys. Rev. Lett. **97**, 132301 (2006).
[8] M. Bleicher *et al.*, Phys. Lett. **B530**, 81 (2002).
[9] M. Bleicher, Nucl. Phys. **A715**, 85 (2003).
[10] G. Torrieri *et al.*, Phys. Lett. **B509**, 239 (2001).
[11] J. Rafelski, J. Letessier, and G. Torrieri, Phys. Rev. C **64**, 054907 (2001).
[12] J. Rafelski, J. Letessier, and G. Torrieri, Phys. Rev. C **65**, 069902 (2002).
[13] C. Markert *et al.*, hep-ph/0206260.
[14] G. E. Brown and M. Rho, Phys. Rev. Lett. **66**, 2720 (1991).
[15] R. Rapp, Nucl. Phys. **A725**, 254 (2003).
[16] E. V. Shuryak and G. Brown, Nucl. Phys. **A717**, 322 (2003).
[17] J. Schaffner-Bielich, Phys. Rev. Lett. **84**, 3261 (2000).
[18] R. Rapp and J. Wambach, Adv. Nucl. Phys. **25**, 1 (2000).
[19] D. Antreasyan, J. W. Cronin, H. J. Frisch, M. J. Shochet, L. Kluberg, P. A. Piroue, and R. L. Sumner, Phys. Rev. D **19**, 764 (1979).
[20] M. Anderson *et al.*, Nucl. Instrum. Methods Phys. Res. A **499**, 659 (2003).
[21] C. Adler *et al.*, Nucl. Instrum. Methods Phys. Res. A **461**, 337 (2001).
[22] K. H. Ackermann *et al.*, Nucl. Instrum. Methods Phys. Res. A **499**, 713 (2003).
[23] J. Adams *et al.*, Phys. Rev. Lett. **91**, 072304 (2003).
[24] B. I. Abelev *et al.*, nucl-ex/0609021.
[25] H. Bichsel, Nucl. Instrum. Methods Phys. Res. A **562**, 154 (2006).
[26] C. Amsler *et al.*, Phys. Lett. **B667**, 1 (2008).
[27] C. Adler *et al.*, Phys. Lett. **B595**, 143 (2004).
[28] C. Adler *et al.*, Phys. Rev. Lett. **89**, 092301 (2002).
[29] X. N. Wang and M. Gyulassy, Phys. Rev. D **44**, 3501 (1991); Comput. Phys. Commun. **83**, 307 (1994).
[30] C. Adler *et al.*, Phys. Rev. Lett. **89**, 272302 (2002).
[31] P. Braun-Munzinger (private communication).
[32] P. F. Kolb and M. Prakash, Phys. Rev. C **67**, 044902 (2003).
[33] C. Adler *et al.*, Phys. Rev. Lett. **87**, 112303 (2001).
[34] M. Aguilar-Benitez *et al.*, Z. Phys. C **50**, 405 (1991).
[35] P. Fachini, R. S. Longacre, Z. Xu, and H. Zhang, J. Phys. G **34**, 431 (2007).
[36] P. D. Acton *et al.*, Z. Phys. C **56**, 521 (1992).
[37] G. D. Lafferty, Z. Phys. C **60**, 659 (1993) (private communication).
[38] K. Ackerstaff *et al.*, Eur. Phys. J. C **5**, 411 (1998).
[39] D. Buskulic *et al.*, Z. Phys. C **69**, 379 (1996).
[40] P. Abreu *et al.*, Phys. Lett. **B298**, 236 (1993).
[41] B. I. Abelev *et al.*, Phys. Rev. C **75**, 064901 (2007).
[42] R. Arndt, J. M. Ford, and L. D. Roper, Phys. Rev. D **32**, 1085 (1985); R. Rapp (private communication).
[43] L. McLerran and R. Venugopalan, Phys. Rev. D **59**, 094002 (1999).
[44] Y. V. Kovchegov and L. McLerran, Phys. Rev. D **60**, 054025 (1999); **62**, 019901(E) (2000).
[45] F. Gelis and A. Peshier, Nucl. Phys. **A697**, 879 (2002).
[46] Y. V. Kovchegov and A. H. Mueller, Nucl. Phys. **B529**, 451 (1998).
[47] A. Dumitru and L. McLerran, Nucl. Phys. **A700**, 492 (2002).
[48] D. Kharzeev and M. Nardi, Phys. Lett. **B507**, 121 (2001).
[49] A. Kovner, L. McLerran, and H. Weigert, Phys. Rev. D **52**, 6231 (1995).
[50] A. Krasnitz and R. Venugopalan, Phys. Rev. Lett. **86**, 1717 (2001).
[51] B. Alper *et al.*, Nucl. Phys. **B87**, 19 (1975).
[52] K. Alpgard *et al.*, Phys. Lett. **B107**, 310 (1981).
[53] G. Gatoff and C. Y. Wong, Phys. Rev. D **46**, 997 (1992).
[54] J. Schaffner-Bielich *et al.*, nucl-th/0202054.
[55] STAR Collaboration (in preparation).
[56] J. Adams *et al.*, Phys. Lett. **B637**, 161 (2006).
[57] J. Adams *et al.*, Phys. Lett. **B616**, 8 (2005).
[58] J. Adams *et al.*, Phys. Rev. Lett. **92**, 112301 (2004).
[59] J. Adams *et al.*, Phys. Rev. C **70**, 064907 (2004).
[60] X. N. Wang, Phys. Rep. **280**, 287 (1997); M. Lev and B. Petersson, Z. Phys. C **21**, 155 (1983); T. Ochiai *et al.* Prog. Theor. Phys. **75**, 288 (1986).
[61] B. I. Abelev *et al.*, Phys. Lett. **B655**, 104 (2007).